Alma Mater Studiorum · Università di Bologna

Dipartimento di Fisica e Astronomia "Augusto Righi"
Corso di Laurea in Fisica

GW-BSE X-ray Absorption Spectra of Small Molecules: Benchmarking Approximations and Basis Sets

Relatrice:
Prof. Margherita Marsili

Presentata da:
Riccardo Imolesi

Anno Accademico 2025/2026

Contents

Sommario

La presente tesi analizza il calcolo di spettri di fotoassorbimento di valenza e di core di piccole molecole nell'ambito della teoria perturbativa a molti corpi. Particolare attenzione è dedicata all'approssimazione GW e all'equazione di Bethe-Salpeter (BSE). Lo scopo è valutare l'affidabilità e l'accuratezza di scelte computazionali e approssimazioni comuni nella descrizione degli stati eccitati. Lo studio è condotto su H_2O, CH_4 e C_2H_4 utilizzando il codice MOLGW sul supercomputer Leonardo del CINECA. A partire da una descrizione della struttura elettronica ottenuta con la teoria del funzionale densità, si calcolano le energie di quasiparticella con l'approssimazione GW per gli stati di valenza e di core. Gli spettri di valenza sono analizzati nell'approssimazione RPA@DFT, che trascura l'attrazione schermata elettrone-lacuna, e successivamente confrontati con calcoli BSE completi. Tale confronto evidenzia il ruolo essenziale dell'interazione attrattiva elettrone-lacuna nel determinare le energie delle eccitazioni neutre. Si discutono la convergenza dei risultati e la loro dipendenza dal funzionale di scambio e correlazione, dalla base gaussiana, dal numero di stati virtuali e dal trattamento delle correzioni di quasiparticella. L'analisi mostra l'importanza delle funzioni diffuse per descrivere accuratamente gli stati non occupati e che le eccitazioni discrete a bassa energia convergono bene rispetto alla dimensione della base. Sono inoltre esaminate le approssimazioni scissor e di Tamm-Dancoff (TDA) e confrontate con la BSE per valutarne accuratezza e convenienza computazionale. Il confronto mostra che la TDA riproduce fedelmente gli spettri BSE per i sistemi considerati, mentre la correzione scissor rigida descrive meno accuratamente gli effetti di quasiparticella dipendenti dallo stato elettronico. Nel complesso, il lavoro fornisce un benchmark di calcoli GW-BSE per gli spettri di assorbimento ottico e near-edge X-ray di sistemi molecolari finiti.

Abstract

The present thesis investigates the calculation of valence and core-level photoabsorption spectra of small molecules within many-body perturbation theory, with a particular focus on the GW approximation and the Bethe-Salpeter equation (BSE). The purpose of this work is to assess the reliability and accuracy of selected computational choices and approximations commonly involved in the description of excited-state properties. The study is carried out on H_2O, CH_4 and C_2H_4 using the MOLGW code on the Leonardo supercomputer hosted by CINECA. Starting from a Density Functional Theory description of the electronic structure, quasiparticle energies are computed within the GW approximation for both valence and core levels. Valence spectra are first analysed within the RPA@DFT approximation, in which the screened electron-hole attraction is neglected, and are subsequently compared with full BSE calculations. This comparison highlights the essential role of the attractive electron-hole interaction in determining neutral excitation energies. The convergence of the results and their dependence on the exchange-correlation functional, Gaussian basis set, number of virtual states and treatment of quasiparticle corrections are systematically discussed. The analysis highlights the importance of diffuse basis functions for an accurate description of unoccupied states and shows that the lowest bound excitations converge well with respect to basis-set size. The Tamm-Dancoff and scissor approximations are also examined and compared with the full BSE. The comparison shows that the Tamm-Dancoff approximation closely reproduces the full BSE spectra for the systems considered, whereas a rigid scissor correction provides a more limited description of state-dependent quasiparticle effects. Overall, this work provides a benchmark of GW-BSE calculations for optical and near-edge X-ray absorption spectra of finite molecular systems.

Chapter 1

Background and motivation

Photoabsorption spectroscopy is one of the most powerful techniques to study the electronic structure of matter. When a photon is absorbed by a system, an electron is promoted from an occupied state to an empty one, and the measured photoabsorption cross section is an indicator of both the energies of the accessible excited states and the strength with which the field couples with them. Depending on the photon energy, different regions of the electronic structure can be probed and investigated. For instance, photons in the ultraviolet and visible range excite valence electrons, since these are weakly bound. When the electronic screening is particularly effective, a single-particle picture holds, and light promotes an electron to an empty state while the rest of the system remains close to its ground state. However, often the interaction between the excited electron and the hole it leaves behind is not negligible, and this is especially true in X-ray spectroscopy, where photons promote electrons from a deep core level. Indeed, the resulting state is a genuinely excited non-ground-state configuration in which the electron-hole interaction strongly reshapes the spectrum. A reliable description of this phenomenon requires a framework that can take into consideration both this interaction and the quasiparticle energies: within the many-body perturbation theory, this is achieved by combining the GW approximation, which corrects the single-particle energies, and the Bethe-Salpeter equation, which describes the electron-hole interaction. Since core binding energies depend strongly on the atomic number and core orbitals are spatially localized around a nucleus, X-ray absorption provides both elemental and local sensitivity. This property is exploited by the near-edge X-ray absorption fine structure spectroscopy (NEXAFS), which probes the region close to an absorption edge where transitions towards low-lying unoccupied states carry information about the local electronic structure of the atom.
The interest in X-ray absorption techniques has increased with the development of ultrafast X-ray sources which have made time-resolved measurements possible. In a typical pump-probe experiment, first an optical pulse promotes the molecule, initiating a photoprocess, then a delayed X-ray pulse probes the evolving system promoting a core electron into the transiently modified valence manifold. Since the X-ray probe is sensitive

to the specific element and the local electronic structure, spectra recorded at different pump-probe delays can provide a direct description of the reorganization of the electrons occurring during this process.
The motivation for the present thesis is related to the development of time-resolved NEXAFS (TR-NEXAFS). A recent real-time approach [1] computes NEXAFS spectra by propagating the time-dependent Schrödinger equation in the space of molecular electronic states, either starting from the ground state or an excited one. In such work, the electronic states are obtained from linear-response time-dependent density functional theory (TDDFT). Furthermore, within the Tamm-Dancoff approximation (TDA), each excited state, whether of valence or core, is written as a linear combination of configurations in which a single electron has been promoted to an empty orbital. Probing a valence-excited state with an X-ray pulse requires the transition dipole moments between the two sets of states, which are obtained from separate TDDFT calculations. Since these two manifolds have the same singly excited form, these dipoles can be reconstructed *a posteriori*. Given that this formulation requires a generic singly excited ansatz, it is not intrinsically embedded in TDDFT: the BSE provides a formally analogous representation, in terms of the electron-hole configurations, which allows it to be used within the same propagation scheme, even if its physical content is different. In TDDFT the electron-hole interaction is described through an exchange-correlation kernel, while the BSE@GW scheme includes the screened electron-hole interaction explicitly: this is what makes it suitable when such an effect acts on the spectrum and is not negligible [2]. In [3] excited states obtained at the GW-BSE level have been used as a basis for the real-time propagation of molecular electronic dynamics, suggesting a natural way to replace the TDDFT description in the TR-NEXAFS framework with a GW-BSE-based one.
However, before such a transition can be made, the GW-BSE calculations in the frequency domain must be well understood, since their accuracy relies on several choices: the Gaussian basis must appropriately describe the unoccupied states, the number of virtual states used impacts both the GW and the BSE excitation energies, and the results depend on the exchange-correlation functional chosen as starting point. Furthermore, approximations such as the TDA and the scissor are commonly used to reduce the computational cost, and hence their accuracy needs to be investigated.
This is precisely what the present thesis aims to assess. No new formalism is introduced and no new code is developed: well known many-body perturbation theory methods and the MOLGW code are used to benchmark both valence and core-level photoabsorption spectra of H_2O, CH_4 and C_2H_4. Since these systems are well known and characterised, they are used as controlled benchmarks, with the purpose of identifying a reliable and transferable setup, providing the frequency-domain foundation required before GW-BSE excited states can be used as input for real-time calculations. Finally, the theoretical framework and the computational methods are introduced in chapter 2, in chapter 3 the results are presented and discussed, and chapter 4 summarizes the main points of this thesis.

Chapter 2

Methods

In this chapter, the theoretical framework underlying this thesis is introduced, along with the computational methods used for the calculations. First, the many-body problem and the Born-Oppenheimer approximation are presented, and then Density Functional Theory is introduced. Second quantization is developed as a tool to go beyond the limitations of standard mean-field approaches, paving the way for many-body perturbation theory through the single-particle Green function, Hedin's equations, and the GW approximation for charged excitations. The Bethe-Salpeter equation is then introduced to account for electron-hole interactions and accurately model neutral excitations, optical absorption, and core-level spectra. Finally, the computational details required for the practical calculations are discussed.

2.1 The many-body problem

Consider a system composed of N electrons and M atomic nuclei: its properties are fully described by the many-body wave function $\phi(\mathbf{r}, \mathbf{R})$, where $\mathbf{r} = \{\mathbf{r}_i\}$ and $\mathbf{R} = \{\mathbf{R}_I\}$ are, respectively, the electronic and ionic coordinates, with lowercase indices i, j running over electrons and uppercase I, J over ions. The wave function obeys the time-independent Schrödinger equation

$$\hat{H}\phi(\mathbf{r}, \mathbf{R}) = E_{\text{tot}}\phi(\mathbf{r}, \mathbf{R}),$$

where the Hamiltonian operator $\hat{H}$ can be written as

$$\hat{H} = \underbrace{\sum_{i=1}^{N} \frac{\mathbf{p}_i^2}{2m}}_{T_e} + \underbrace{\sum_{I=1}^{M} \frac{\mathbf{P}_I^2}{2M_I}}_{T_I} + \underbrace{\sum_{i<j} \frac{e^2}{|\mathbf{r}_i - \mathbf{r}_j|}}_{V_{ee}} - \underbrace{\sum_{i,I} \frac{Z_I e^2}{|\mathbf{r}_i - \mathbf{R}_I|}}_{V_{Ie}} + \underbrace{\sum_{I<J} \frac{Z_I Z_J e^2}{|\mathbf{R}_I - \mathbf{R}_J|}}_{V_{II}}, \tag{2.1}$$

where T_e and T_I are the kinetic energy of the electrons and ions, V_{ee} the electron-electron Coulomb repulsion, V_{Ie} the ion-electron interaction and finally V_{II} is the ion-ion repulsion. Although exact in principle, finding a direct solution is computationally extraordinarily hard given the enormous amount of particles and interactions involved ($N \sim 10^{23}$), as the wave function depends on $3N + 3M$ spatial coordinates.
A first simplification comes from the Born-Oppenheimer approximation: since the nuclei are much heavier than electrons, the former can be treated adiabatically, as their dynamics are negligibly slow on the timescale of electronic motion. Within the Born-Oppenheimer approximation, the wave function takes a factorized form

$$\phi(\mathbf{r}, \mathbf{R}) = \psi(\mathbf{r}, \mathbf{R})\chi(\mathbf{R}),$$

in which the nuclei coordinates are treated as parameters rather than dynamical variables. One then solves the electronic Schrödinger problem alone

$$(T_e + V_{ee} + V_{Ie})\psi = E_{\mathbf{R}}\psi,$$

where the nuclear static-potential effect is reflected in the parametric dependence of $E_{\mathbf{R}}$ on $\mathbf{R}$.

2.1.1 The independent-particle approximation

Even after applying the Born-Oppenheimer approximation, solving the electronic Schrödinger equation remains a complicated task. A widely adopted strategy consists in replacing the fully interacting Hamiltonian with an effective Hamiltonian of *non-interacting* particles

$$\hat{H}_0 = \sum_i \hat{H}_i,$$

so that the many-body wave function factorizes into a product of single-particle wave functions $\psi(\mathbf{r}_1, \ldots, \mathbf{r}_N, t) = \psi_1(\mathbf{r}_1, t) \cdots \psi_N(\mathbf{r}_N, t)$, each satisfying an independent Schrödinger equation

$$i\hbar \frac{\partial \psi_i}{\partial t} = \hat{H}_i \psi_i.$$

Starting from the interacting Hamiltonian $\hat{H} = T_e + V_{Ie} + V_{ee}$, one introduces an auxiliary one-body potential $\mathcal{V}_i$ and rewrites the Hamiltonian as

$$\hat{H} = \underbrace{\left(\sum_i -\frac{\hbar^2}{2m}\nabla_i^2 + V_{\text{ext}}(\mathbf{r}_i) + \mathcal{V}_i \right)}_{\hat{H}_0} + \underbrace{\left(\frac{1}{2}\sum_{i \neq j} v_{ee}(|\mathbf{r}_i - \mathbf{r}_j|) - \mathcal{V}_i \right)}_{\hat{H}_{\text{res}}},$$

where $V_{\text{ext}} := V_{Ie}$ is the external ionic potential. The point of view adopted is hence that the external ionic potential defines the problem. Now, for a judicious choice of $\mathcal{V}_i$, the

residual term $\hat{H}_{\text{res}}$ is small and can be treated perturbatively. This is the essence of the *mean-field* approach.
There exists a variational formulation of the mean-field method that can be performed over single-particles wave functions of the electrons in their ground state. This method encompasses the Hartree and Hartree-Fock approximation, and Density Functional Theory (DFT), which provides an exact mapping of the initial problem onto a non-interacting problem. In DFT the approximations are confined to the exchange-correlation potential, whose explicit form will be discussed in the following sections. [4, 5]

2.2 Density Functional Theory

DFT provides an exact reformulation of the many-body electronic problem in terms of the ground state electron density $n(\mathbf{r})$, rather than the full many-body wave function $\psi(\mathbf{r}_1, \ldots, \mathbf{r}_N)$. The rigorous foundation of this approach rests on the theorems of Hohenberg and Kohn [6], presented in section 2.2.1, while the practical self-consistent scheme due to Kohn and Sham is discussed in sections 2.2.2 and 2.2.3.

2.2.1 The Hohenberg-Kohn theorem

Before stating and proving the Hohenberg-Kohn theorem, it is worth mentioning that the proof - and hence the theorem itself - is restricted to the class of *v-representable* densities, i.e. all the N-electron ground state densities that are associated with an external potential. Now, the idea underlying the Hohenberg-Kohn theorem is the following. For a given external potential $V_{\text{ext}}(\mathbf{r})$, the Schrödinger equation yields a ground-state wave function $\psi(\mathbf{r})$. From this wave function, it is possible to extract the corresponding ground-state density $n(\mathbf{r})$.
One then has a surjective function that maps the set of external potentials onto the set of the v-representable ground state densities,

$$V_{\text{ext}}(\mathbf{r}) \longrightarrow n(\mathbf{r})$$

and can, hopefully, invert it. This is exactly what the Hohenberg-Kohn theorem allows one to do, up to a constant.

Theorem (Hohenberg-Kohn theorem)**.** *Let $n(\mathbf{r})$ be the ground-state electron density of a system of N interacting electrons subject to an external potential V_{ext}. Then V_{ext} is uniquely determined, up to an additive constant, by $n(\mathbf{r})$.*

Proof. The proof proceeds by *reductio ad absurdum* and consists of two parts. Assume that $V^{(1)}_{\text{ext}}(\mathbf{r})$ and $V^{(2)}_{\text{ext}}(\mathbf{r})$ are two external potentials differing by more than an additive constant, which yield the same ground-state density $n(\mathbf{r})$. Let E_1, E_2 be their respective ground-state energies, and ψ_1, ψ_2 the corresponding ground-state wave functions.

First, one shows that $\psi_1 \neq \psi_2$. Assume for contradiction that $\psi_1 = \psi_2 := \psi$. Then both Schrödinger equations are satisfied:

$$(T_e + V_{ee} + V_{\text{ext}}^{(1)})\psi = E_1\psi, \qquad (T_e + V_{ee} + V_{\text{ext}}^{(2)})\psi = E_2\psi.$$

Subtracting the second from the first gives

$$(V_{\text{ext}}^{(1)} - V_{\text{ext}}^{(2)})\psi = (E_1 - E_2)\psi.$$

Since $\psi(\mathbf{r}) \neq 0$ almost everywhere[1], this implies

$$V_{\text{ext}}^{(1)}(\mathbf{r}) - V_{\text{ext}}^{(2)}(\mathbf{r}) = E_1 - E_2,$$

which is a constant, contradicting the hypothesis. Hence $\psi_1 \neq \psi_2$.
Now, since $\psi_1 \neq \psi_2$, the Rayleigh-Ritz variational principle gives a strict inequality: ψ_2 cannot be the ground-state wave function of $\hat{H}^{(1)}$, hence

$$\begin{aligned} E_1 &= \langle\psi_1|\hat{H}^{(1)}|\psi_1\rangle \\ &< \langle\psi_2|\hat{H}^{(1)}|\psi_2\rangle \\ &= \langle\psi_2|\hat{H}^{(2)} + V_{\text{ext}}^{(1)} - V_{\text{ext}}^{(2)}|\psi_2\rangle \\ &= E_2 + \int \left[V_{\text{ext}}^{(1)}(\mathbf{r}) - V_{\text{ext}}^{(2)}(\mathbf{r})\right] n(\mathbf{r})\, d\mathbf{r}. \end{aligned}$$

Exchanging the roles of the two systems, one gets:

$$E_2 < E_1 + \int \left[V_{\text{ext}}^{(2)}(\mathbf{r}) - V_{\text{ext}}^{(1)}(\mathbf{r})\right] n(\mathbf{r})\, d\mathbf{r}.$$

Finally, adding the two inequalities gives

$$E_1 + E_2 < E_1 + E_2,$$

which is a clear contradiction. □

First of all, it is noticeable that the proof does not assume the non-degeneracy of any ground state, which makes it pretty general. An immediate corollary of this theorem is that the ground-state density $n(\mathbf{r})$ carries the full information about the system: it uniquely determines the external potential V_{ext}, which in turn determines the Hamiltonian, and hence every observable $\hat{O}$ is a unique functional of $n(\mathbf{r})$. If one makes the

[1] In the language of real analysis, *almost everywhere* means except possibly on a set of Lebesgue measure zero.

assumption that the ground state is non-degenerate [2], the wave function itself is a functional of n, i.e. $\psi = \psi[n]$ and it is possible to define the *universal functional*

$$F[n] = \langle \psi[n] | V_{ee} + T_e | \psi[n] \rangle \tag{2.2}$$

which can be used to define the total energy functional, often denoted as just energy functional:

$$E[n] = F[n] + \int V_{\text{ext}}(\mathbf{r}) n(\mathbf{r}) d\mathbf{r}.$$

A fundamental pillar of DFT is the following variational principle, often presented as the second Hohenberg-Kohn theorem.

Theorem. *The total energy functional attains its minimum at the ground state energy E_0, which is obtained by minimizing $E[n]$ over all v-representable densities. Moreover, the minimizing density is precisely the ground state density $n_0(\mathbf{r})$.*

$$E_0 = \min E[n] = \min \left\{ \langle \psi | V_{ee} + T_e | \psi \rangle + \int V_{ext}(\mathbf{r}) n(\mathbf{r}) d\mathbf{r} \right\} \tag{2.3}$$

Proof. Let n_0 be the ground state density associated with the potential $V_{\text{ext}}(\mathbf{r})$ and $\psi[n_0]$ its corresponding wave function. Let furthermore $n(\mathbf{r})$ be the ground state density associated with another potential $V(\mathbf{r})$ and $\psi[n]$ its corresponding wave function. By the Rayleigh-Ritz variational principle,

$$E_0 = \langle \psi[n_0] | \hat{H} | \psi[n_0] \rangle \leqslant \langle \psi[n] | \hat{H} | \psi[n] \rangle$$

now, expanding the right-hand side

$$\langle \psi[n] | \hat{H} | \psi[n] \rangle = F[n] + \int V_{\text{ext}}(\mathbf{r}) n(\mathbf{r}) d\mathbf{r} = E[n]$$

so that finally one gets

$$E_0 = E[n_0] \leqslant E[n].$$

□

[2] This assumption is a very delicate one. In fact, in the presence of degenerate ground states, the map $V_{\text{ext}}(\mathbf{r}) \mapsto n(\mathbf{r})$ is not single-valued, since distinct degenerate ground states can correspond to different densities. Likewise, the mapping $n(\mathbf{r}) \mapsto \psi[n]$ breaks down, as multiple distinct wave functions within the degenerate subspace can yield the same density. The universal functional $F[n]$ can nonetheless be shown to exist via the *weaker joint degeneracy* and *internal-energy* theorems [7] or alternatively through the Levy-Lieb constrained-search construction, which bypasses the issue entirely [8–10].

2.2.2 The Exchange-Correlation potential

Despite the formal exactness of the Hohenberg-Kohn theorem, the direct minimization of $E[n]$ remains, in practice, an intractable problem. This is due to the fact that, while the Hohenberg-Kohn theorem guarantees the existence of $F[n]$, its exact form is not known, and in particular no simple and accurate expression exists for the kinetic energy as a functional of the electron density. The main insight of the Kohn-Sham approach is to bypass this obstacle by reformulating the variational problem rather than trying to approximate $F[n]$ directly.
Consider an *auxiliary system* of N non-interacting electrons that has, obviously, a different Hamiltonian yet produces the same density as the original system

$$n(\mathbf{r}) = n'(\mathbf{r}) = \sum_{i}^{occ} |\psi_i|^2.$$

It is possible to decompose the universal functional as

$$F[n] = T'[n] + E_{\mathrm{H}}[n] + E_{\mathrm{xc}}[n]$$

where $T'[n]$ is the non-interacting kinetic energy, $E_{\mathrm{H}} = \frac{e^2}{2} \iint \frac{n(\mathbf{r})n(\mathbf{r}')}{|\mathbf{r}-\mathbf{r}'|} d\mathbf{r}d\mathbf{r}'$ the Hartree electrostatic energy and finally E_{xc} is the exchange-correlation functional, defined as the exact remainder between the true universal functional $F[n]$ and its decomposition in the auxiliary system:

$$E_{xc}[n] := (T_e[n] - T'[n]) + (V_{ee}[n] - E_H[n]). \tag{2.4}$$

It is worth emphasizing that no approximation has been introduced at this stage: the definition above is mathematically exact. Yet it is precisely here that one's ignorance about the many-body problem is concentrated, since the explicit dependence of E_{xc} on $n(\mathbf{r})$ remains unknown.
The total energy functional then reads

$$E[n] = T'[n] + E_H[n] + E_{xc}[n] + \int V_{\mathrm{ext}}(\mathbf{r})n(\mathbf{r})d\mathbf{r}.$$

Minimizing[3] $E[n]$ together with the constraint $\int n(\mathbf{r})d\mathbf{r} = N$, enforced via the Lagrange multiplier μ[4], yields the stationarity condition

$$\frac{\delta T'[n]}{\delta n(\mathbf{r})} + V_{\mathrm{H}}(\mathbf{r}) + V_{\mathrm{xc}}(\mathbf{r}) + V_{\mathrm{ext}}(\mathbf{r}) = \mu \tag{2.5}$$

[3]Functional derivatives are defined implicitly: $\delta F = F[f + \delta f] - F[f] = \int \frac{\delta F[f]}{\delta f(x)} \delta f(x) dx$.

[4]It also turns out that μ is the chemical potential, indeed the stationarity condition is the functional equivalent of the thermodynamic definition $\mu = \frac{\partial U}{\partial N}$.

where the Hartree potential and the exchange-correlation potential are introduced as functional derivatives of the respective energy contributions,

$$V_H(\mathbf{r}) = \frac{\delta E_H[n]}{\delta n(\mathbf{r})} = e^2 \int \frac{n(\mathbf{r}')}{|\mathbf{r} - \mathbf{r}'|} d\mathbf{r}', \qquad V_{xc}(\mathbf{r}) = \frac{\delta E_{xc}[n]}{\delta n(\mathbf{r})}$$

This stationarity condition is formally identical to that of a non-interacting electron gas moving in the Kohn-Sham effective potential

$$V_{KS}(\mathbf{r}) = V_{\text{ext}}(\mathbf{r}) + V_H(\mathbf{r}) + V_{xc}(\mathbf{r}).$$

This observation is the key that unlocks the self-consistent single-particle scheme that will be discussed in the following section.

2.2.3 Kohn-Sham equations

The stationarity condition derived above is formally identical to that of a system of N non-interacting electrons moving in the effective potential $V_{KS}(\mathbf{r})$. In this auxiliary system, the wave function is a Slater determinant $\psi = \frac{1}{\sqrt{N!}}[\psi_i(r_j)]$, the Hamiltonian can be written as $H = \sum_i h_i$ and in order for the relation $H\psi = E\psi$ to hold, it is necessary that each wave function satisfies the single-particle Schrödinger equation. The ground-state density of the original interacting system can then be obtained by solving a set of such equations, the *Kohn-Sham equations*,[5]

$$\left(-\frac{\hbar^2}{2m}\nabla^2 + V_{KS}(\mathbf{r})\right)\psi_i(\mathbf{r}) = \varepsilon_i \psi_i(\mathbf{r}), \tag{2.6}$$

where the Kohn-Sham orbitals $\{\psi_i\}$ reconstruct the ground-state density via

$$n(\mathbf{r}) = \sum_i^{\text{occ}} |\psi_i(\mathbf{r})|^2.$$

Since V_{KS} depends on $n(\mathbf{r})$, and $n(\mathbf{r})$ depends in turn on the orbitals $\{\psi_i\}$, equation (2.6) must be solved *self-consistently*: one starts from an initial guess for the density $n^{(0)}(\mathbf{r})$, constructs $V_{KS}^{(0)}$, solves the eigenvalue problem to obtain a new set of orbitals and hence a new density $n^{(1)}(\mathbf{r})$. This procedure is then iterated until convergence, i.e. until $||n^{(k+1)} - n^{(k)}|| < \tau$, τ being the chosen tolerance.
The Kohn-Sham scheme then provides a huge advantage: all the many-body problem complexity is confined to the single term $E_{xc}[n]$, for which controlled approximations can be constructed [4]. Once an approximation for E_{xc} is chosen, the many-body problem is reduced to N independent single-particle problems, which are far easier to solve computationally.

[5]The eigenvalues ε_i arise as Lagrange multipliers enforcing the orthonormality constraint $\langle\psi_i|\psi_j\rangle = \delta_{ij}$ when varying $E[n]$ with respect to the orbitals $\{\psi_i\}$ [5]. They should therefore not be interpreted as physical single-particle energies in general.

2.2.4 Approximations for the exchange-correlation functional

The scope of this section is to provide an overview of the most widely used approximations for the exchange-correlation functional, presented in order of increasing complexity, computational cost, and accuracy.

Local density approximation

The simplest approximation for the exchange-correlation functional is the Local density approximation (LDA), which was first introduced by Kohn and Sham [11], defined by

$$E_{\mathrm{xc}}^{\mathrm{LDA}} = \int n(\mathbf{r})\varepsilon_{\mathrm{xc}}(n(\mathbf{r}))d\mathbf{r}$$

which means that the system is treated locally as a homogeneous electron gas - whose exchange-correlation energy per particle is precisely $\varepsilon_{\mathrm{xc}}$ - with density n. One then typically writes $\varepsilon_{\mathrm{xc}} = \varepsilon_{\mathrm{x}} + \varepsilon_{\mathrm{c}}$, separating the exchange and the correlation terms. While the former is analytically known - for a homogeneous electron gas - to be

$$\varepsilon_{\mathrm{x}} = -\frac{3}{4}(\frac{3}{\pi})^{1/3}n^{1/3}(\mathbf{r}),$$

ε_{c} has no analytical form, and is in practice obtained by Quantum Monte Carlo methods[6]. The main reason that makes LDA so accurate for certain calculations - particularly for systems with slowly varying densities - is that it fulfils the sum rule for the exchange-correlation hole. To see this, one defines the pair density as

$$n_2(\mathbf{r},\mathbf{r}') = N(N-1)\int |\Psi(\mathbf{r},\mathbf{r}',\mathbf{r}_3,\ldots,\mathbf{r}_N)|^2 d\mathbf{r}_3\cdots d\mathbf{r}_N$$

which represents the probability of finding one electron at $\mathbf{r}$ and another at $\mathbf{r}'$. The exchange-correlation hole h_{xc} is then defined by

$$n_2(\mathbf{r},\mathbf{r}') = n(\mathbf{r})n(\mathbf{r}') + n(\mathbf{r})h_{\mathrm{xc}}(\mathbf{r},\mathbf{r}')$$

and represents the deficit of electronic density at $\mathbf{r}'$ due to the presence of an electron at $\mathbf{r}$. Integrating over $\mathbf{r}'$ and using the normalization of n_2, one obtains the exact sum rule:

$$\int h_{\mathrm{xc}}(\mathbf{r},\mathbf{r}')d^3r' = -1$$

The exchange-correlation energy is then expressible as

$$E_{\mathrm{xc}}[n] = \frac{1}{2}\int \frac{n(\mathbf{r})h_{\mathrm{xc}}(\mathbf{r},\mathbf{r}')}{|\mathbf{r}-\mathbf{r}'|}d\mathbf{r}d\mathbf{r}'$$

[6]See [12] for the original QMC calculation of the homogeneous electron gas, and [13] for its parametrization into a closed-form expression suitable for practical use.

Since this integral depends only on the spherical average of h_{xc}, and not on its detailed shape, the LDA yields surprisingly accurate results as long as the sum rule is satisfied. However, it systematically overestimates the binding energy of molecules and underestimates lattice parameters, which motivates the need for improved approximations.

Generalized Gradient Approximation

The natural extension of the LDA is the Generalized Gradient Approximation (GGA), which improves upon it by allowing $\varepsilon_{\mathrm{xc}}$ to depend not only on the local density $n(\mathbf{r})$, but also on its gradient $\nabla n(\mathbf{r})$:

$$E_{\mathrm{xc}}^{\mathrm{GGA}}[n] = \int n(\mathbf{r})\varepsilon_{\mathrm{xc}}(n(\mathbf{r}), \nabla n(\mathbf{r}))d^3r$$

making this a *semi-local* approximation for the exchange-correlation functional. A naive gradient expansion of $\varepsilon_{\mathrm{xc}}$ in powers of $|\nabla n|$ turns out to worsen the results with respect to LDA, as it violates the sum rule on n_{xc}. The GGA instead constructs $\varepsilon_{\mathrm{xc}}$ by enforcing a set of known exact constraints, which the LDA already satisfies, plus additional ones. One of the most widely used GGA functionals is that of Perdew, Burke and Ernzerhof [14], known as PBE. Rather than expanding $\varepsilon_{\mathrm{xc}}$ in powers of $|\nabla n|$, PBE constructs it by enforcing a set of known exact physical constraints, yielding more accurate binding energies and lattice parameters than LDA.

Hybrid functionals

The key idea behind hybrid functionals consists of calculating the correlation energy using approximated DFT functionals, while the exchange part is treated exactly via the Hartree-Fock exchange energy $E_{\mathrm{x}}^{\mathrm{HF}}$, which is known analytically:

$$E_{\mathrm{xc}}^{\mathrm{hyb}} = \alpha E_{\mathrm{x}}^{\mathrm{HF}} + (1-\alpha)E_{\mathrm{x}}^{\mathrm{GGA}} + E_{\mathrm{c}}^{\mathrm{GGA}}$$

where α is the fraction of exact exchange. Two of the most widely used hybrid functionals are PBE0, which incorporates a fraction $\alpha = 1/4$ of exact exchange, and BHLYP, which uses a larger fraction $\alpha = 1/2$. The higher fraction of exact exchange in BHLYP makes it generally more suitable for systems with a strong exchange character, whereas PBE0 is regarded as a reliable general-purpose functional.

2.3 Elements of second quantization

The description of a system of N identical particles in terms of (anti)symmetric wave functions becomes increasingly cumbersome as N grows, since the symmetry constraint under particle exchange must be imposed by hand on every state and on every operator.

For example, a Slater determinant built from N orbitals already requires $N!$ terms when written explicitly as a product of one-particle states. This motivates the introduction of *second quantization*, a formalism in which the symmetry properties of identical particles are automatically encoded in the algebraic properties of a small set of operators, while all many-body states and operators take a simpler and more compact form. Consider now a set of fermions, and let $\{|\psi_k\rangle\}$ be a complete orthonormal basis of the single-particle Hilbert space, with wave functions $\psi_k(x) = \langle x|\psi_k\rangle$, where $x = (\mathbf{r}, \sigma)$ collects both the position and spin coordinates and k comprises an orbital and a spin quantum number. Accordingly, we use the notation $\int dx \equiv \sum_\sigma \int d\mathbf{r}$. A convenient way to label the N-particle basis states is through their *occupation numbers* $n_k \in \{0, 1\}$, specifying how many particles occupy each orbital ψ_k:

$$|n_1, n_2, \ldots\rangle.$$

The vector space spanned by all such basis states for any number of particles, including the zero-particle state, forms the so-called *Fock space*. For each orbital ψ_k one introduces a *creation operator* $\hat{a}_k^\dagger$ and an *annihilation operator* $\hat{a}_k$, defined through their action on this occupation-number basis,

$$\hat{a}_k^\dagger|n_1, \ldots, n_k, \ldots\rangle = \begin{cases} (-1)^{\sum_{i=1}^{k-1} n_i}|n_1, \ldots, n_k + 1, \ldots\rangle & n_k = 0 \\ 0 & n_k = 1, \end{cases}$$

$$\hat{a}_k|n_1, \ldots, n_k, \ldots\rangle = \begin{cases} (-1)^{\sum_{i=1}^{k-1} n_i}|n_1, \ldots, n_k - 1, \ldots\rangle & n_k = 1 \\ 0 & n_k = 0, \end{cases}$$

so that $\hat{a}_k^\dagger$ adds a particle to orbital k and $\hat{a}_k$ removes one, while the sign factor $(-1)^{n_1+\ldots+n_{k-1}}$ accounts for the reordering of the antisymmetric wave function. One can verify directly that operators defined in this way satisfy the relations

$$\left\{\hat{a}_k, \hat{a}_{k'}^\dagger\right\} = \delta_{kk'}, \qquad \left\{\hat{a}_k, \hat{a}_{k'}\right\} = \left\{\hat{a}_k^\dagger, \hat{a}_{k'}^\dagger\right\} = 0, \tag{2.7}$$

where $\{\hat{A}, \hat{B}\} := \hat{A}\hat{B} + \hat{B}\hat{A}$ denotes the anticommutator. These relations are the algebraic counterpart of the properties of identical fermions: from $(\hat{a}_k^\dagger)^2 = \frac{1}{2}\left\{\hat{a}_k^\dagger, \hat{a}_k^\dagger\right\} = 0$ it follows that two fermions cannot occupy the same orbital, recovering the Pauli exclusion principle, while $\hat{a}_k^\dagger\hat{a}_{k'}^\dagger = -\hat{a}_{k'}^\dagger\hat{a}_k^\dagger$ encodes the antisymmetry of the wave function under particle exchange. Introducing the *vacuum* $|0\rangle$, the state with no particles, satisfying $\hat{a}_k|0\rangle = 0$ for all k, it follows that any N-particle Slater determinant built from orbitals $k_1 < k_2 < \cdots < k_N$ can be written as

$$|\psi_{k_1} \ldots \psi_{k_N}\rangle = \hat{a}_{k_1}^\dagger \cdots \hat{a}_{k_N}^\dagger|0\rangle.$$

The anticommutation relations (2.7) automatically guarantee that this state vanishes if two quantum numbers coincide and changes sign under exchange of any two of them,

without any further bookkeeping; the full antisymmetrization that would be required in first quantization is here a direct consequence of the algebra of the $\hat{a}_k$ and $\hat{a}_k^\dagger$ operators. It is finally possible to define the *occupation operator* $\hat{n}_k \equiv \hat{a}_k^\dagger \hat{a}_k$ that counts the number of particles in orbital ψ_k[7], and its sum over all orbitals gives the number operator

$$\hat{N} = \sum_k \hat{n}_k. \tag{2.8}$$

The advantage of this formalism becomes fully apparent when one rewrites the many-body electronic Hamiltonian within the Born-Oppenheimer approximation,

$$\hat{H} = \sum_{j=1}^{N} \left(-\frac{\hbar^2}{2m}\nabla_j^2 + V_{\text{ext}}(\mathbf{r}_j) \right) + \frac{1}{2}\sum_{j\neq j'} v(\mathbf{r}_j, \mathbf{r}_{j'}),$$

[8] where the first term collects the kinetic energy and the external ionic potential, and the second term is the two-body Coulomb repulsion $v(\mathbf{r}, \mathbf{r}') = e^2/|\mathbf{r} - \mathbf{r}'|$, summed over all distinct pairs of particles. This operator depends explicitly on N, and its action on antisymmetric many-body wave functions requires enforcing the exchange symmetry explicitly. It is possible to show that in second quantization such a Hamiltonian takes the compact, and N-independent, form

$$\hat{H} = \sum_{k,k'} \langle \psi_k | \hat{T} + \hat{V}_{\text{ext}} | \psi_{k'} \rangle \hat{a}_k^\dagger \hat{a}_{k'} + \frac{1}{2}\sum_{k,q}\sum_{k',q'} \langle \psi_q \psi_k | \hat{v} | \psi_{k'} \psi_{q'} \rangle \hat{a}_q^\dagger \hat{a}_k^\dagger \hat{a}_{q'} \hat{a}_{k'}, \tag{2.9}$$

where the only operators appearing are the creation and annihilation operators introduced above. All the remaining quantities are just complex numbers, given by the matrix elements of the one- and two-body parts of the Hamiltonian in the chosen orbital basis,

$$\langle \psi_k | \hat{T} + \hat{V}_{\text{ext}} | \psi_{k'} \rangle = \int \psi_k^*(x) \left(-\frac{\hbar^2}{2m}\nabla^2 + V_{\text{ext}}(\mathbf{r}) \right) \psi_{k'}(x) dx, \tag{2.10}$$

$$\langle \psi_q \psi_k | \hat{v} | \psi_{k'} \psi_{q'} \rangle = \int \psi_q^*(x) \psi_k^*(x') v(\mathbf{r}, \mathbf{r}') \psi_{k'}(x) \psi_{q'}(x') dx dx', \tag{2.11}$$

underlining the careful ordering of the annihilation operators $\hat{a}_{q'}\hat{a}_{k'}$ in equation (2.9), which is the reverse of the order in which k' and q' appear in the matrix element (2.11), since the operators do not commute. The most remarkable feature of equation (2.9) is that it assumes the same algebraic form in every particle-number subset of the Fock space: all the N-dependence is absorbed into the operators $\hat{a}_k, \hat{a}_k^\dagger$ acting directly on the Fock space, rather than appearing explicitly in the Hamiltonian.

[7] It is possible to prove that, for fermions, $\hat{n}^2 = \hat{n}$, i.e. it is a projection operator (or it is idempotent, using the language of linear algebra), from which it follows that its only eigenvalues are 0 and 1.

[8] $v(\mathbf{r})$ is exactly what we called v_{ee} in section 2.1.1.

2.3.1 Field operators

It is often convenient to express the language of second quantization in a representation that is independent of the particular choice of the single-particle basis. In order to do so, one introduces the *field operators*

$$\hat{\psi}(x) = \sum_k \psi_k(x)\hat{a}_k,$$
$$\hat{\psi}^\dagger(x) = \sum_k \psi_k^*(x)\hat{a}_k^\dagger,$$

where the sum runs over all the allowed values of the quantum number k. The field operators are therefore nothing but the creation and annihilation operators expressed in the continuous position-spin basis. This means that $\hat{\psi}$ and $\hat{\psi}^\dagger$ respectively annihilate and create a particle at the position-spin point x, i.e., in the generalized position eigenstate $|x\rangle$. Using equation (2.7) and the completeness relation $\sum_k \psi_k(x)\psi_k^*(x') = \delta(x - x')$, it follows that

$$\left\{\hat{\psi}(x), \hat{\psi}^\dagger(x')\right\} = \delta(x - x'), \qquad \left\{\hat{\psi}(x), \hat{\psi}(x')\right\} = \left\{\hat{\psi}^\dagger(x), \hat{\psi}^\dagger(x')\right\} = 0. \tag{2.12}$$

In terms of the field operators, it is natural to define $\hat{n}(x) = \hat{\psi}^\dagger(x)\hat{\psi}(x)$, from which it follows that the number operator reads

$$\hat{N} = \int \hat{n}(x)dx, \tag{2.13}$$

and it is possible to rewrite the Hamiltonian in equation (2.9) in the simpler form

$$\hat{H} = \int \hat{\psi}^\dagger(x)\left[\hat{T}(\mathbf{r}) + V_{\text{ext}}(\mathbf{r})\right]\hat{\psi}(x)dx + \frac{1}{2}\int \hat{\psi}^\dagger(x)\hat{\psi}^\dagger(x')v(\mathbf{r},\mathbf{r}')\hat{\psi}(x')\hat{\psi}(x)dxdx'. \tag{2.14}$$

Now, since the Hamiltonian does not depend explicitly on time, the dynamics of the system is generated by the evolution operator $\hat{U}(t) = e^{-i\hat{H}t/\hbar}$, and the field operators can be evolved in the Heisenberg picture,

$$\hat{\psi}(x,t) = e^{i\hat{H}t/\hbar}\hat{\psi}(x)e^{-i\hat{H}t/\hbar}, \qquad \hat{\psi}^\dagger(x,t) = e^{i\hat{H}t/\hbar}\hat{\psi}^\dagger(x)e^{-i\hat{H}t/\hbar},$$

where they satisfy the anticommutation relations (2.12) at equal times. The Heisenberg-picture field operators $\hat{\psi}(x,t), \hat{\psi}^\dagger(x,t)$ are the basic objects of what will follow: the single-particle Green function will be defined precisely as a ground-state expectation value of their time-ordered products, while the number operator (2.13) and the Coulomb integrals (2.11) will be the starting point for constructing the self-energy Σ and the screened interaction W through Hedin's equations.

2.4 Elements of many-body perturbation theory

The previous sections introduced density functional theory as a practical path to ground-state properties, obtained by solving an effective single-particle problem. However, excited-state properties such as electronic gaps and optical spectra require a treatment that goes beyond a static, local single-particle potential. This section first introduces linear response theory, which defines the response function χ, and its general analytic properties, and then the framework needed to actually compute it, which is then developed within many-body perturbation theory, built around the concept of the Green function and its perturbative expansion.

2.4.1 Linear response theory

The Kohn-Sham eigenvalues are, strictly speaking, Lagrange multipliers with no direct physical meaning as quasiparticle energies, and the Hohenberg-Kohn theorem, while establishing a one-to-one correspondence between the external potential and the ground-state density, says nothing about excited states. The appropriate framework for computing optical properties is *linear response theory*, which describes how a system in its ground state reacts to a small external perturbation. In the optical regime, the perturbation is the oscillating electric field of an electromagnetic wave, and the response is the induced polarization of the electronic charge distribution.
In quantum mechanics, such a perturbation is introduced by adding a source term to the Hamiltonian,

$$H'(t) = H_0 - Q\phi(t)$$

where Q is a Hermitian observable of the system and $\phi(t)$ is a controllable external field. The goal of linear response theory is to determine how the expectation value of Q changes in the presence of $\phi(t)$. Now, if the perturbation is sufficiently weak, the change is linear in the applied field:

$$\delta\langle Q(t)\rangle = \int_{-\infty}^{+\infty} \chi(t,t')\phi(t')dt'$$

where $\chi(t,t')$ is defined to be the *linear response function* of the system. If one assumes stationarity, then it must be $\chi(t,t') = \chi(t-t')$, whereas causality requires that

$$\chi(t-t') = 0 \qquad \text{for } t < t'$$

This has a precise consequence in terms of frequency. Taking the inverse Fourier transform

$$\chi(t) = \int_{-\infty}^{+\infty} \frac{d\omega}{2\pi}\chi(\omega)e^{-i\omega t}$$

causality implies $\chi(t) = 0$ for $t < 0$. Closing the contour with a semicircle of radius $R \to \infty$ in the upper half-plane $\mathrm{Im}(\omega) > 0$, the contribution of the large semicircle

vanishes by Jordan's lemma.[9] The condition $\chi(t) = 0$ for $t < 0$ is satisfied only if $\chi(\omega)$ has no singularities in the upper half-plane. Hence, $\chi(\omega)$ is holomorphic for $\mathrm{Im}(\omega) > 0$.

2.4.2 Kramers-Kronig relations

A fundamental consequence of the analyticity of $\chi(\omega)$ in the upper half-plane is that its real and imaginary parts are not independent. To derive their relation, one needs a preliminary result from complex analysis. Consider an integral of the form

$$\int_{-\infty}^{+\infty} \frac{f(x)}{x - x_0} dx$$

where $f(x)$ is regular on the real axis and x_0 is a real point. Since the integrand diverges at $x = x_0$, the integral is not defined in the ordinary sense. One gives it a meaning by deforming the contour to pass either above or below the singularity with a small semicircle $\gamma_\pm$ of radius $\varepsilon \to 0$. Since x_0 is a simple pole of the integrand, one can write

$$\frac{f(z)}{z - x_0} = \frac{f(x_0)}{z - x_0} + g(z)$$

where $g(z)$ is regular at x_0. By the small circle lemma, the contribution of $g(z)$ to the semicircular integral vanishes as $\varepsilon \to 0$. The contribution from the singular part is, using the parametrization $z = x_0 + \varepsilon e^{i\theta}$:

$$\int_{\gamma_\pm} \frac{f(z)}{z - x_0} dz \xrightarrow{\varepsilon \to 0} \mp i\pi f(x_0)$$

where the upper sign refers to γ_+ (above) and the lower to γ_- (below). Taking the limit $\varepsilon \to 0$ for the full integral, the two pieces excluding the semicircle define the *Cauchy principal value*:

$$\mathcal{P} \int_{-\infty}^{+\infty} \frac{f(x)}{x - x_0} dx \equiv \lim_{\varepsilon \to 0} \left[\int_{-\infty}^{x_0 - \varepsilon} \frac{f(x)}{x - x_0} dx + \int_{x_0 + \varepsilon}^{+\infty} \frac{f(x)}{x - x_0} dx \right]$$

Equivalently, instead of deforming the contour, one can displace the pole off the real axis by replacing $x_0 \to x_0 \mp i\varepsilon$, which yields the same result. Combining the principal value with the semicircular contribution, one obtains the *Sokhotski-Plemelj formula*:

$$\lim_{\varepsilon \to 0} \int_{-\infty}^{+\infty} \frac{f(x)}{x - x_0 \pm i\varepsilon} dx = \mathcal{P} \int_{-\infty}^{+\infty} \frac{f(x)}{x - x_0} dx \mp i\pi f(x_0)$$

[9] Actually, Jordan's lemma also requires $\chi(\omega) \to 0$ as $|\omega| \to \infty$. Throughout this thesis it is assumed that $\chi(t) \to 0$ as $t \to \infty$, which corresponds to the physical situation in which the system returns to its unperturbed state once the external field is switched off. This condition also ensures that $\chi(\omega) \to 0$ as $|\omega| \to \infty$, making Jordan's lemma applicable.

or, in the compact distributional form

$$\lim_{\varepsilon\to 0}\frac{1}{x-x_0\pm i\varepsilon}=\mathcal{P}\left(\frac{1}{x-x_0}\right)\mp i\pi\delta(x-x_0)$$

Now, since $\chi(\omega)$ is holomorphic in the upper half-plane and vanishes as $|\omega|\to\infty$, consider the contour integral

$$\oint_C \frac{\chi(\omega')}{\omega'-\omega}d\omega'=0$$

where C runs along the real axis, indented upward with a small semicircle γ_+ of radius $\varepsilon\to 0$ around $\omega'=\omega$, and closes with a large semicircle of radius $R\to\infty$ in the upper half-plane. The integral vanishes because χ has no poles inside C. Since $\chi(\omega')\to 0$ as $|\omega'|\to\infty$, the contribution of the large semicircle vanishes as $R\to\infty$. The small semicircle γ_+ contributes $-i\pi\chi(\omega)$. What remains is the principal value integral along the real axis,

$$\mathcal{P}\int_{-\infty}^{+\infty}\frac{\chi(\omega')}{\omega'-\omega}d\omega'-i\pi\chi(\omega)=0$$

hence

$$\chi(\omega)=\frac{1}{i\pi}\mathcal{P}\int_{-\infty}^{+\infty}\frac{\chi(\omega')}{\omega'-\omega}d\omega'$$

Separating real and imaginary parts of the equation above, $\chi(\omega)=\chi_1(\omega)+i\chi_2(\omega)$, one gets the *Kramers-Kronig relations*:

$$\chi_1(\omega)=\frac{1}{\pi}\mathcal{P}\int_{-\infty}^{+\infty}\frac{\chi_2(\omega')}{\omega'-\omega}d\omega'$$

$$\chi_2(\omega)=-\frac{1}{\pi}\mathcal{P}\int_{-\infty}^{+\infty}\frac{\chi_1(\omega')}{\omega'-\omega}d\omega'$$

These relations are essentially consequence of causality alone, and hold for any response function. Their physical meaning is profound: the dissipative part $\chi_2(\omega)$, which governs energy absorption, and the reactive part $\chi_1(\omega)$, which describes the non-dissipative response, are not independent, as each determines the other completely through a principal value integral over the whole range of frequencies.

2.4.3 The single-particle Green function

For a time-independent Hamiltonian $\hat{H}$[10], the Schrödinger equation is formally solved by $|\psi(t)\rangle=e^{-iH(t-t_0)/\hbar}|\psi(t_0)\rangle$. The Green function, or propagator, is the time evolution

[10]Throughout this section, $\hat{H}$ denotes a single-particle Hamiltonian with eigenvalues E_n and eigenstates $\{\psi_n(x)\}$.

operator written in the position representation,

$$G(x, x_0; t - t_0) = \langle x | e^{-iH(t-t_0)/\hbar} | x_0 \rangle,$$

and represents the probability amplitude for finding the particle at x at time t, given that it was at x_0 at time t_0. By inserting the resolution of identity, one gets

$$G(x, x_0; t - t_0) = \sum_n e^{-iE_n(t-t_0)/\hbar} \psi_n(x) \psi_n^*(x_0),$$

which shows that G encodes the full spectral information of the Hamiltonian H.
It is convenient to distinguish propagation forward and backward in time by introducing the *retarded* and *advanced* Green functions[11]

$$G^+(t - t_0) = \theta(t - t_0) e^{-iH(t-t_0)/\hbar}, G^-(t - t_0) = -\theta(t_0 - t) e^{-iH(t-t_0)/\hbar},$$

which describe the evolution towards the future and towards the past, respectively. Consider the Fourier transform of the retarded Green function with respect to time,

$$G^+(E) = \frac{1}{i\hbar} \int_{-\infty}^{+\infty} e^{iEt/\hbar} G^+(t) dt = \frac{1}{i\hbar} \int_0^{+\infty} e^{iEt/\hbar} G^+(t) dt$$

it is clear that the integral does not converge absolutely, as it oscillates without damping as $t \to \infty$. The divergence is regularized by giving the energy a small positive imaginary part, $E \to E + i\eta$, which makes the integral absolutely convergent and yields

$$G^+(E) = \lim_{\eta \to 0^+} \frac{1}{i\hbar} \int_0^{\infty} e^{i(E+i\eta-H)t/\hbar} dt = \lim_{\eta \to 0^+} \frac{1}{E + i\eta - H}.$$

For the advanced Green function the integration runs over $t < 0$, so convergence requires $E \to E - i\eta$. Putting these together,

$$G^{\pm}(E) = \lim_{\eta \to 0^+} \frac{1}{E \pm i\eta - H}.$$

The sign of $\pm i\eta$ thus directly encodes the direction of propagation in time, a distinction that is also present in the sign of the infinitesimal imaginary parts accompanying the poles of the Lehmann representation. Since H is self-adjoint, its spectrum is real, and all the singularities of $G^+(E)$ lie in the lower half of the complex energy plane; closing the integration contour in the upper half-plane, one verifies that $G^+(t)$ indeed vanishes for $t < 0$, as causality requires. It is also possible to see that $G^+(E)$ and $G^-(E)$ are boundary values of a single analytic function of the complex variable z, the *resolvent*

$$G(z) = \frac{1}{z - H},$$

[11] It is worth noting that these are operators, whereas the definition above is a matrix element in the position representation.

which is analytic everywhere except on the spectrum of $\hat{H}$: discrete eigenvalues appear as poles, whereas the continuous spectrum produces a branch cut on the real axis. If the Hamiltonian is split as the sum of an exactly solvable Hamiltonian and an interaction term, $\hat{H} = \hat{H}_0 + \hat{H}_I$, then the *Dyson equation* yields

$$G(z) = G_0(z) + G_0(z)H_I G(z), \qquad G_0(z) = \frac{1}{z - H_0},$$

which can be solved iteratively, generating a perturbative series in H_I. An analogous structure will emerge in the many-body problem discussed in the following sections. The Green function G is related to a non-interacting one G_0 by a Dyson equation of the same form, $G = G_0 + G_0 \Sigma G$, where Σ is the *self-energy*, an effective, energy-dependent operator that encodes all exchange and correlation effects - playing the role of the interaction term H_I[12].

2.4.4 The single-particle Green function in second quantization

The Green function introduced in the previous section can be generalized to the many-body context by replacing the position eigenstates with the field operators, and the evolution amplitude with a ground-state expectation value. The single-particle Green function is defined as the ground-state expectation value of the time-ordered product of two field operators in the Heisenberg picture,

$$G(1,2) = -i\langle \Psi_0 | \mathcal{T}\{\hat{\psi}(1)\hat{\psi}^\dagger(2)\} | \Psi_0 \rangle, \tag{2.15}$$

[13] where $|\Psi_0\rangle$ is the normalized ground state of the interacting N-electron system, and the compact notation

$$1 \equiv (x_1, t_1) = (\mathbf{r}_1, \sigma_1, t_1)$$

is used. From now on natural units with $\hbar = 1$ are adopted, in order to simplify the formal expression of many-body perturbation theory. It is worth mentioning that $\mathcal{T}$[14] introduces a minus sign for each transposition of fermionic operators,

$$\mathcal{T}[\hat{\psi}(1)\hat{\psi}^\dagger(2)] = \begin{cases} \hat{\psi}(1)\hat{\psi}^\dagger(2), & t_1 > t_2 \\ -\hat{\psi}^\dagger(2)\hat{\psi}(1), & t_1 < t_2. \end{cases} \tag{2.16}$$

[12] A deeper and more detailed discussion of the Green function can be found in [15].

[13] The prefactor $-i$ is purely a convention, it is also possible to define G without the prefactor: the two definitions differ by an overall factor $-i$ and clearly describe the same physics, but using different conventions can turn out to be tricky.

[14] $\mathcal{T}$ is the time-ordering operator, and can be defined rigorously as $\mathcal{T}[A(t_1)B(t_2)\dots Z(t_n)] = \sum_P \theta(t_{P_1}, t_{P_2}, \dots, t_{P_n}) A(t_{P_1})B(t_{P_2})\dots Z(t_{P_n})$, where the sum is over all the permutations of $1, 2, \dots, n$ and $\theta(t_1, t_2, \dots, t_n) = \prod_{i=1}^{n-1} \theta(t_i - t_{i+1}) = \theta(t_1 - t_2)\theta(t_2 - t_3)\dots\theta(t_{n-1} - t_n)$ is a generalisation of the Heaviside function.

The crucial difference with respect to the single-particle case of the previous section is that the amplitude is now evaluated on the ground state of the fully interacting N-electron system, rather than on an eigenstate of a one-body Hamiltonian.
Definition (2.15) hence describes both electron and hole propagation: for $t_1 > t_2$, the operator $\hat{\psi}^\dagger(2)$ adds an electron in x_2 at time t_2, and $\hat{\psi}(1)$ removes it at the later time t_1: the Green function then describes the propagation of an added electron from 2 to 1, through a system that reorganizes in response to its presence. In contrast, for $t_1 < t_2$, an electron is first removed at 1, leaving a hole behind, which is subsequently filled at 2: the Green function then describes the propagation of a hole.

2.4.5 The Lehmann representation

The physical content of equation (2.15) becomes explicit once the field operators are expanded over a complete set of eigenstates of the Hamiltonian. Since $\hat{\psi}^\dagger$ adds an electron to the system and $\hat{\psi}$ removes one, the states that contribute to the sum are not those of the N-electron system, but the eigenstates $|\Psi_i^{N+1}\rangle$ and $|\Psi_i^{N-1}\rangle$ of the systems with one electron more and one electron less, with energies E_i^{N+1} and E_i^{N-1}. It is therefore natural to introduce a single index i running over the excited states of both systems, and to associate with it the energy

$$E_i = \begin{cases} E_i^{N+1} - E_0^N, & E_i > \mu \\ E_0^N - E_i^{N-1}, & E_i < \mu, \end{cases} \tag{2.17}$$

where μ is the chemical potential of the system, and E_0^N is the ground-state energy. These are called addition (or removal) energies[15], as they describe the energy required to add an electron to the system and the energy required to remove one, and they are separated by μ, since the inequality $E_{\text{removal}} \leq \mu \leq E_{\text{addition}}$ holds for any system. Accordingly, one defines the *Lehmann amplitudes*

$$f_i(x) = \begin{cases} \langle \Psi_0 | \hat{\psi}(x) | \Psi_i^{N+1} \rangle, & E_i > \mu \\ \langle \Psi_i^{N-1} | \hat{\psi}(x) | \Psi_0 \rangle, & E_i < \mu, \end{cases} \tag{2.18}$$

which measure the overlap between the ground state with one electron added (removed) at the point x and the i-th eigenstate of the $(N \pm 1)$-electron system.
With these definitions, inserting the resolution of the identity between the two field operators in equation (2.15) and writing the Heisenberg operators explicitly, the Green function takes the form

$$iG(x_1, x_2; t_1 - t_2) = \sum_i \left[\theta(t_1 - t_2)\theta(E_i - \mu) - \theta(t_2 - t_1)\theta(\mu - E_i)\right] f_i(x_1) f_i^*(x_2) e^{-iE_i(t_1 - t_2)}, \tag{2.19}$$

[15]It is also worth mentioning that these, in contrast with the E_n of section 2.4.3, are not eigenvalues of a single-particle Hamiltonian, but reduce to them in the non-interacting limit.

where the two Heaviside functions select, for each time ordering, only the states that can actually contribute to the sum. The Green function depends on the time difference alone, and can therefore be Fourier transformed with respect to $t_1 - t_2 = \tau$. Just as in the single-particle case discussed in the previous section, the exponentials do not decay as $|\tau| \to \infty$, and the integral is regularized by giving the frequency an infinitesimal imaginary part η, whose sign is fixed by the direction of propagation in time: a positive η is needed for the addition energies, ($\tau > 0$), and a negative one for the removal energies ($\tau < 0$). The result is the *Lehmann representation* of the Green function,

$$G(x_1, x_2; \omega) = \sum_i \frac{f_i(x_1) f_i^*(x_2)}{\omega - E_i + i\eta \mathrm{sgn}(E_i - \mu)} \tag{2.20}$$

which constitutes the main result of this section. The poles of G are located at the exact electron addition and removal energies E_i of the interacting system, defined in equation (2.17), and both are directly comparable to what is measured in photoemission experiments. This is a great advantage compared to the Kohn-Sham eigenvalues ε_i, which do not carry any explicit physical meaning. Equation (2.20) also shows that the poles of G lie infinitesimally close to the real axis, below it for $E_i > \mu$ and above it for $E_i < \mu$, so that the chemical potential separates the two regions[16].
Applying the Sokhotski-Plemelj formula derived in section 2.4.2 to equation (2.20) one obtains

$$\mathrm{Im}G(x_1, x_2; \omega) = \pi \mathrm{sgn}(\mu - \omega) \sum_i f_i(x_1) f_i^*(x_2) \delta(\omega - E_i),$$

which shows that the sign of ImG is a general property of the Green function, as it is positive below μ and negative above it. Since the sign of ImG changes across μ, such quantity cannot itself be interpreted as a density of states. Compensating for the sign change, one defines the *spectral function*, which is positive for all frequencies, and can therefore be interpreted as a sort of density[17] of available addition and removal states, weighted by the Lehmann amplitudes:

$$A(x_1, x_2; \omega) = \frac{1}{\pi} \mathrm{sgn}(\mu - \omega) \mathrm{Im}G(x_1, x_2; \omega) = \sum_i f_i(x_1) f_i^*(x_2) \delta(\omega - E_i), \tag{2.21}$$

It is furthermore possible to prove that A encodes the same information that G does and that it satisfies the sum rule

$$\int_{-\infty}^{\infty} A(x_1, x_2, \omega) d\omega = \delta(x_1 - x_2)$$

[16]The discrete pole structure of the Lehmann representation is a consequence of the finite size of the system. In an extended system the excitations form a continuum, the sum becomes an integral, and the poles merge into a branch cut on the real axis, as [16] and [17] show. The molecules studied in this thesis are finite systems, and their spectra therefore consist of discrete peaks rather than continuous bands.

[17]See [16].

as a consequence of the completeness of the states with $N-1$ and $N+1$ electrons and the anticommutation relations between $\psi^\dagger$ and ψ, see [18].

2.4.6 The Dyson equation and the self-energy

Despite its usefulness and its deep physical meaning, the Lehmann representation does not provide insight into how to actually obtain the information contained in G, since the many-body eigenstates entering equation (2.18) are not known. To make progress, one has to look at how G evolves in time. Taking the derivative of equation (2.15) with respect to t_1, and using the Heisenberg equation of motion for the field operators generated by the Hamiltonian (2.14) together with the anticommutation relations (2.12), one obtains[18]

$$\left(i\frac{\partial}{\partial t_1} - h(\mathbf{r}_1)\right) G(1,2) + i\int d3\; v(1,3)G_2(1,3^+;2,3^{++}) = \delta(1,2), \tag{2.22}$$

[19] where $h(\mathbf{r}) = \hat{T}(\mathbf{r}) + V_{\text{ext}}(\mathbf{r})$ is the one-electron Hamiltonian already appearing in equation (2.14), $v(1,3) = v(\mathbf{r}_1,\mathbf{r}_3)\delta(t_1-t_3)$ is the instantaneous Coulomb interaction, $\delta(1,2) = \delta(x_1-x_2)\delta(t_1-t_2)$, and the notation 3^+ denotes the space-spin-time point 3 with its time argument augmented by a positive infinitesimal quantity. The truly new object appearing in equation (2.22) is the *two-particle Green function*

$$G_2(1,2;1',2') = -\langle\Psi_0|\mathcal{T}\big\{\hat{\psi}(1)\hat{\psi}(2)\hat{\psi}^\dagger(2')\hat{\psi}^\dagger(1')\big\}|\Psi_0\rangle, \tag{2.23}$$

which, just like $G(1,2)$, describes the propagation of a pair of particles, of a pair of holes, or of a particle and a hole, depending on the time ordering of its arguments. Now, equation (2.22) is exact, but it is not a closed equation: the equation of motion of G involves G_2 and, were one to write the equation of motion of G_2, it would in turn involve the three-particle Green function, and so on. What comes out is an infinite hierarchy of coupled equations, in which the complexity of the original many-body problem is entirely preserved: the knowledge of the N-particle Green function would eventually be required. It is nevertheless possible to extract some information. Consider the case in which the two particles propagate independently of each other, which means that G_2 factorizes into $G_2(1,3^+;2,3^{++}) \simeq G(1,2)G(3,3^+)$. Choosing $t_2 = t_1^+$ in the definition (2.15) selects the second line of equation (2.16), so that $-iG(3,3^+) = \langle\Psi_0|\hat{\psi}^\dagger(x_3)\hat{\psi}(x_3)|\Psi_0\rangle = n(x_3)$ is the electron density. This contribution therefore reads

$$i\int d3\; v(1,3)G(1,2)G(3,3^+) = -\left[\int dx_3\; v(\mathbf{r}_1,\mathbf{r}_3)n(x_3)\right] G(1,2) = -V_H(\mathbf{r}_1)G(1,2),$$

[18] The time derivative acts both on the field operator $\hat{\psi}(1)$ and on the Heaviside functions implicit in $\mathcal{T}$; the latter produce a $\delta(t_1-t_2)$ that multiplies the equal-time anticommutator $\{\hat{\psi}(x_1),\hat{\psi}^\dagger(x_2)\} = \delta(x_1-x_2)$, which is the origin of the right-hand side.

[19] The full derivation of equation 2.22 can be found in [19].

which is exactly the Hartree potential described in section 2.2.2, i.e. the classical electrostatic potential generated by the total electron density, felt by the propagating particle. Being proportional to $G(1,2)$, this term combines with $-h(\mathbf{r}_1)G(1,2)$, already present on the left-hand side of equation (2.22), promoting the one-electron Hamiltonian h to the *Hartree Hamiltonian*

$$h_H(\mathbf{r}) = h(\mathbf{r}) + V_H(\mathbf{r}) = \hat{T}(\mathbf{r}) + V_{\text{ext}}(\mathbf{r}) + V_H(\mathbf{r}), \tag{2.24}$$

which describes an electron moving in the field of the nuclei and in the average electrostatic field of all the other electrons, treated as a static charge distribution, which is the mean-field picture of section 2.1.1.
What is left of the two-particle term is, by definition, the *self-energy* Σ. It is defined as the operator that, acting on G, reproduces all the effects the Hartree term does not include,

$$\int d3\ \Sigma(1,3)G(3,2) \ = \ -i \int d3\ v(1,3)\Big[G_2(1,3^+;2,3^{++}) - G(1,2)G(3,3^+)\Big]. \tag{2.25}$$

Equation (2.25) shows that the square bracket is the deviation of the "true" two-particle Green function from the independent propagation of the two particles, which is exactly the correlation between the propagating particle and the other electrons. Its physical content is that the particle added to the system rearranges the charge distribution around itself, and then feels the potential generated by that very rearrangement. Just as in DFT, no approximation has been introduced so far: the definition is exact, and all the ignorance about the many-body problem is now concentrated in a single unknown object.
With these definitions, the equation of motion (2.22) becomes

$$\left(i\frac{\partial}{\partial t_1} - h_H(\mathbf{r}_1)\right) G(1,2) - \int d3\ \Sigma(1,3)G(3,2) = \delta(1,2), \tag{2.26}$$

which involves G but not G_2, and hence closes the hierarchy. Let now G_H denote the Green function of the Hartree Hamiltonian, defined by

$$\left(i\frac{\partial}{\partial t_1} - h_H(\mathbf{r}_1)\right) G_H(1,2) = \delta(1,2),$$

so that G_H is formally the functional inverse of the operator $i\partial_{t_1} - h_H$ or, in the frequency space,

$$G_H^{-1}(x_1,x_2;\omega) = \delta(x_1 - x_2)\left[\omega - h_H(\mathbf{r}_1)\right]. \tag{2.27}$$

The first term of the left-hand side of equation (2.26) can then be rewritten as $\int d3 G_H^{-1}(1,3)G(3,2)$, so that the whole equation reads

$$\int d3\ \Big[G_H^{-1}(1,3) - \Sigma(1,3)\Big]G(3,2) = \delta(1,2).$$

Multiplying this expression from the left by G_H and integrating, one finally obtains the *Dyson equation*

$$G(1,2) = G_H(1,2) + \int d3d4\; G_H(1,3)\Sigma(3,4)G(4,2), \tag{2.28}$$

or, equivalently, in the frequency domain,

$$G^{-1}(x_1, x_2; \omega) = G_H^{-1}(x_1, x_2; \omega) - \Sigma(x_1, x_2; \omega). \tag{2.29}$$

Equation (2.28) has exactly the same structure as the Dyson equation encountered in section 2.4.3. Knowing G_H, which is a mean-field quantity, together with an approximation for Σ, one obtains the interacting Green function and, through the Lehmann representation, the exact addition and removal energies of the system.
The self-energy is therefore the object connecting the mean-field system to the interacting one, but its properties are considerably less convenient than those of the Kohn-Sham exchange-correlation potential. As is evident from equation (2.25), Σ is non-local in space, spin and time, so that it enters the equations through an integral rather than as a multiplicative factor. Moreover, the closure of the hierarchy is only formal: equation (2.25) defines Σ in terms of G_2, which is what we tried to eliminate, and Σ is itself a functional of G, so that its determination requires, in principle, a self-consistent procedure.
It is finally worth mentioning that the mean-field approximations previously discussed are recovered as particular cases of equation (2.26), depending on how Σ is approximated. If the two particles in G_2 are allowed to propagate independently but their indistinguishability is retained, G_2 acquires, besides the direct term already absorbed into h_H, an exchange term, and the self-energy reduces to the Fock exchange operator, giving the Hartree-Fock approximation. If instead Σ is replaced by a local, static and Hermitian potential $V_{\text{xc}}(\mathbf{r})$, one recovers the Kohn-Sham equations (2.6). This is a qualitative *a posteriori* justification for using Kohn-Sham eigenvalues as approximate excitation energies: V_{xc} is itself an approximation to the exact self-energy. The problem is then reduced to finding a good approximation for Σ, just as the Kohn-Sham scheme reduces the many-body problem to approximating V_{xc}. A more complete and exhaustive treatment of the self-energy and its properties can be found in [16, 18, 20, 21], although these use different conventions in the definition of G and Σ.

2.5 Hedin's equations and the GW approximation

In the previous section it was shown that, on the one hand, the Dyson equation and the definition of the self-energy are exact, and reduce the whole problem to the determination of Σ. On the other hand, Σ was defined through the two-particle Green function G_2,

which is exactly what one was trying to avoid. This means that the problem has not actually been solved: what is still missing is a way to express Σ in terms of computable quantities, and this is what the Hedin's equations provide.

2.5.1 The Schwinger functional derivative

The tool that breaks the hierarchy is the *Schwinger functional derivative technique*. The idea is to probe the system with a small, fictitious external potential U, and set it to zero at the end of the calculation [20]. In the presence of U, the variation of the Green function with respect to the external potential is related to the two-particle Green function by the identity [16, 21]

$$\frac{\delta G(1,2)}{\delta U(3)} = G(1,2)G(3,3^+) - G_2(1,3;2,3^+). \tag{2.30}$$

Here comes the crucial observation: the two-particle Green function that appears in the definition of the self-energy is nothing but a functional derivative of the one-particle Green function with respect to U. This means that G_2, the object that generates the hierarchy and made the problem intractable, has been reduced to a derivative of G, and hence the self-energy can be recast - without any approximation - in a form that does not contain G_2 explicitly anymore. Exploiting this method (repeating the substitution and applying multiple times the chain rule, see [20] for a more complete treatment of this matter), one gets a set of five coupled equations, relating five quantities, called *Hedin's equations*.

2.5.2 Hedin's equations and pentagon

Before writing Hedin's equations down, it is worth introducing the quantities that appear in them alongside G and Σ. Since the self-energy describes the response of the system to the addition or removal of an electron, it must be connected to the way the system behaves under such a perturbation. This is described by the *irreducible polarizability* P[21], which can be pictured as the creation of electron-hole pairs as the electrons rearrange to screen the added charge. Now, the added particle interacts with these electron-hole pairs, and the pairs interact among themselves: the quantity that encodes all such interactions is the *vertex function* Γ. Finally, since every charge is surrounded by this polarization cloud, the effective interaction between two particles is weaker than the bare Coulomb repulsion: it is the *screened interaction* W, which replaces v. Such replacement is not

[20] It is important to stress that U is introduced only as a mathematical device that allows higher-order Green functions to be generated through functional differentiation.

[21] Sometimes the irreducible polarizability is denoted by $\tilde{P}$ to distinguish it from P, the reducible one, the response to the external potential U alone; the two are related by a Dyson equation, $P = \tilde{P} + \tilde{P}vP$. Anyway, only the irreducible one appears in equation (2.33).

purely descriptive: since v is strong, an approximation to the self-energy built directly on the bare Coulomb interaction would be poorly controlled, whereas W is weak, so that approximating Σ in terms of the screened interaction is far more reliable.
As discussed in the previous section, one obtains the closed set of five coupled integral equations relating G, Σ, W, P and Γ, known as Hedin's equations[22] :

$$G(1,2) = G_H(1,2) + \int d3d4\; G_H(1,3)\Sigma(3,4)G(4,2) \tag{2.31}$$

$$\Sigma(1,2) = i \int d3d4\; G(1,3)W(4,1^+)\Gamma(3,2;4) \tag{2.32}$$

$$W(1,2) = v(1,2) + \int d3d4\; v(1,3)P(3,4)W(4,2) \tag{2.33}$$

$$P(1,2) = -i \int d3d4\; G(1,3)G(4,1)\Gamma(3,4;2) \tag{2.34}$$

$$\Gamma(1,2;3) = \delta(1,2)\delta(1,3) + \int d4d5d6d7\; \frac{\delta\Sigma(1,2)}{\delta G(4,5)} G(4,6)G(7,5)\Gamma(6,7;3) \tag{2.35}$$

The first of these is the already known Dyson equation (2.28), the second expresses the self-energy in terms of G, W and Γ; the third is a Dyson equation for the screened interaction W, in which P plays, for W, the same role that Σ plays for G; the fourth gives P and the last defines the vertex through $\delta\Sigma/\delta G$. Each of these equations carries physical meaning [16, 21]. Equation (2.34), $P = -iGG\Gamma$, describes an electron and a hole propagating together (the pair GG), coupled by their interaction through the vertex Γ; and similarly equation (2.32) $\Sigma = iGW\Gamma$ describes a particle (G) interacting with the rest of the system through the screened interaction W and Γ. The vertex Γ carries the information on how the added particle and the electron-hole pairs interact with each other, and its appearance in both P and Σ is what ties this set of equations together, suggesting to solve it through a self-consistent cycle.
In order to do so, the idea is to start from an initial guess for the self-energy, evaluate in turn Γ, P and W, and obtain an updated Σ: this yields, through the Dyson equation, an improved Green function, from which the cycle can begin again. The five quantities and the five equations connecting them are naturally arranged on the *Hedin's pentagon* of figure 2.1, and, carried to self-consistency, this cycle would in principle deliver exactly what one is looking for. This scheme, however, cannot be carried out in practice. The obstacle is the vertex: the evaluation of Γ through $\delta\Sigma/\delta G$ and the integral equation (2.35) is not applicable for any realistic system. This means that it is unavoidable to approximate the vertex.

[22]The remarkable aspect of Hedin's equations is that they allow the reorganization of the infinite hierarchy of Green functions into five coupled equations involving only five quantities.

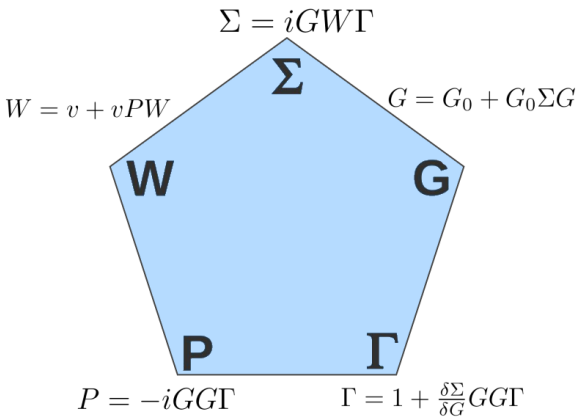

Figure 2.1: Hedin's pentagon

2.5.3 The GW approximation

The simplest way to close the pentagon by approximating Γ is to neglect $\delta\Sigma/\delta G$, so that equation (2.35) becomes

$$\Gamma(1,2;3) \simeq \delta(1,2)\delta(1,3). \tag{2.36}$$

This is referred to as setting the vertex to its interaction-free form, and corresponds to starting the self-consistent cycle from $\Sigma = 0$ or, equivalently, from G_H.
Inserting equation (2.36) into the Hedin's equations for Σ and P, the Dirac deltas remove the integrations, and one obtains

$$\Sigma(1,2) = iG(1,2)W(2,1^+), \tag{2.37}$$

or, more compactly, $\Sigma = iGW$, while the irreducible polarizability reduces to

$$P(1,2) = P^0(1,2) = -iG(1,2)G(2,1), \tag{2.38}$$

or $P = -iGG$. This is the density response of a system of independent particles, i.e. the *random phase approximation* (RPA) to the polarizability, describing an electron and a hole that propagate without interacting with each other [20, 21]. The screened interaction then follows from the third Hedin's equation evaluated with P^0,

$$W(1,2) = v(1,2) + \int d3d4\ v(1,3)P^0(3,4)W(4,2), \tag{2.39}$$

so that, within the GW approximation, W is the RPA-screened Coulomb interaction. The pentagon previously shown then reduces to a four-sided polygon: the vertex is bypassed, and only G, Σ, W and P^0 remain. The physical meaning of equation (2.37) becomes clear once one moves to the frequency domain, where the product $\Sigma = iGW$

becomes a convolution, and W is split into its bare and dynamical parts, $W = v + W_p$ with $W_p := W - v$. The self-energy then separates as

$$\Sigma = \Sigma_x + \Sigma_c = iGv + iGW_p,$$

where $\Sigma_x = iGv$ is static, non-local and has the same form as the Fock exchange operator, so that Hartree-Fock is recovered in the limit $W \to v$, while $\Sigma_c = iGW_p$ is dynamical and encodes correlation [21]. The GW approximation therefore describes an electron interacting with the rest of the system through a repulsion dynamically screened by the polarization cloud it induces around itself.
Although the vertex has been eliminated, equations (2.37)-(2.39) remain coupled to the Dyson equation through G, so that a fully consistent solution would still require iterating the cycle.

2.5.4 The quasiparticle equation

It is useful to make explicit the eigenvalue problem contained in the Dyson equation. Writing equation (2.29) and substituting equation 2.27 in it, one gets that the poles of G, which by the Lehmann representation are the exact addition and removal energies E_i, are the solutions of the *quasiparticle equation*

$$\left(-\frac{1}{2}\nabla^2 + V_{\text{ext}}(\mathbf{r}) + V_H(\mathbf{r})\right)\psi_i(\mathbf{r}) + \int d\mathbf{r}'\, \Sigma(\mathbf{r}, \mathbf{r}'; E_i)\psi_i(\mathbf{r}') = E_i\psi_i(\mathbf{r}), \tag{2.40}$$

where ψ_i are the quasiparticle amplitudes and natural units have been used. Equation (2.40) is formally analogous to the Kohn-Sham equation (2.6), with the crucial difference that the local, static and Hermitian potential $V_{xc}(\mathbf{r})$ has been replaced by the self-energy $\Sigma(\mathbf{r}, \mathbf{r}'; E_i)$, which is non-local, energy-dependent and non-Hermitian[23]. The non-Hermiticity allows the eigenvalues E_i to be complex, in particular their imaginary part is the width of the quasiparticle peak[24].

2.5.5 The GW approximation in practice

Nevertheless, solving the quasiparticle equation (2.40) together with the GW cycle self-consistently is computationally expensive. In practice one relies on the G_0W_0 method, which consists of a single iteration of the cycle performed on top of a mean-field solution, usually the Kohn-Sham one. The starting point is the observation that the quasiparticle Hamiltonian in equation (2.40) and the Kohn-Sham Hamiltonian (2.6) differ only by the replacement of $V_{xc}(\mathbf{r})$ with $\Sigma(\mathbf{r}, \mathbf{r}'; E_i)$. It is therefore reasonable to treat $\Sigma - V_{xc}$ as a perturbation. Projecting equation (2.40) onto ϕ_i^{KS} and subtracting the Kohn-Sham

[23] The Kohn-Sham scheme is recovered with the substitution $\Sigma \to V_{xc}^{KS}(\mathbf{r})$.
[24] A more exhaustive treatment of this matter can be found in [16–18].

equation (2.6), the quasiparticle energy is obtained as a first-order correction to the Kohn-Sham eigenvalue,

$$E_i = \varepsilon_i^{KS} + \left\langle \phi_i^{KS} \middle| \mathrm{Re}\Sigma(E_i) - V_{xc} \middle| \phi_i^{KS} \right\rangle. \tag{2.41}$$

This is what it means that the GW result is a correction on top of a DFT calculation. Equation (2.41) is still implicit, since Σ has to be evaluated at the unknown E_i. The frequency dependence of the self-energy is therefore linearized around the Kohn-Sham eigenvalue ε_i^{KS}, which yields the explicit expression [17, 18],

$$E_i = \varepsilon_i^{KS} + Z_i \left\langle \phi_i^{KS} \middle| \mathrm{Re}\Sigma(\varepsilon_i^{KS}) - V_{xc} \middle| \phi_i^{KS} \right\rangle, \qquad Z_i = \left(1 - \left. \frac{\partial \mathrm{Re}\Sigma}{\partial \omega} \right|_{\varepsilon_i^{KS}} \right)^{-1}, \tag{2.42}$$

where Z_i is the *renormalization factor*[25], which quantifies the spectral weight carried by the quasiparticle peak. It is smaller than one, and approaches unity in finite systems where the dynamical effects in Σ are small [17].
The main limitation of G_0W_0 is its dependence on the starting point: since both G_0 and W_0 are built from the Kohn-Sham orbitals and eigenvalues, the corrected energies inherit a residual dependence on the exchange-correlation functional used in the underlying DFT step. This is why, in this thesis, many G_0W_0 corrections are computed using different functionals (PBE, PBE0 and BHLYP).
A partial way to reduce this dependence is to introduce again some self-consistency, while keeping the vertex fixed to the identity and the wave functions frozen to the Kohn-Sham ones, so that only the eigenvalues are updated and the correction (2.42) is iterated until convergence in energy is reached. In particular, it is possible to distinguish two levels, following the terminology of the code [22] employed in this thesis. These are G_nW_0, in which the updated eigenvalues are reinserted only in the Green function entering Σ, while the screened interaction W_0 is kept fixed; whereas in G_nW_n, they are reinserted in both the Green function and the screening W. In the same terminology, G_0W_0 is often referred to simply as GW.

2.6 Bethe-Salpeter equation and optical properties

The GW approximation is useful as it provides the charged excitations of the system, namely the energy required to add an electron to, or remove one from, the ground state

[25]Since the spectral function is positive and, once projected on a single state, integrates to unity (because of the sum rule of section 2.4.5), its total weight is shared between the quasiparticle peak, carrying the fraction Z_i, and the remaining structures, carrying $1 - Z_i$; hence $0 \leq Z_i \leq 1$. These additional structures are called *satellites*, and arise when the added electron (or hole) couples to other neutral excitations of the system. They are a consequence of the dynamical, frequency-dependent nature of Σ: a static self-energy, such as in Hartree-Fock, produces no satellites [17].

by photoemission. Optical absorption is a different process: the photon promotes an electron to an empty state, but the number of particles in the system remains constant, so that the excited electron and the hole it leaves behind coexist in the system as a mutually interacting pair. It is hence necessary to take into account the electron-hole interaction, which has been previously neglected as $P(1,2) = -iG(1,2)G(2,1)$ within the RPA. This suppresses all *excitonic effects*, such as the redistribution of oscillator strength, that cannot be neglected. Capturing them requires an effective Hamiltonian, the so-called *excitonic Hamiltonian*, and the Bethe-Salpeter equation (BSE).

2.6.1 The Bethe-Salpeter equation

The natural object for describing the coupled propagation of an electron and a hole is the two-particle correlation function, or four-point polarizability $L(1,2;1',2')$, defined as

$$iL(1,2;1',2') = -G_2(1,2;1',2') + G(1,1')\,G(2,2'),$$

which turns out to be very useful as the response measured in absorption is recovered by contracting its indices, $\chi(1,2) = L(1,2;1,2)$. Since no closed equation relating χ and the two-point polarizability exists, it is necessary to calculate $L(1,2;1',2')$ as an intermediate step in such a process. Applying the same Schwinger derivative discussed in section 2.5.1, writing L as a derivative of G with respect to an external potential and eliminating $\delta G^{-1}/\delta U$ through the Dyson equation, one obtains the Bethe-Salpeter equation,

$$L(1,2;1',2') = L_0(1,2;1',2') + \int d(3456)\, L_0(1,4;1',3)\, \Xi(3,6;4,5)\, L(5,2;6,2'), \quad (2.43)$$

where $L_0(1,2;1',2') = -i\,G(1,2')\,G(2,1')$, whose contraction gives back the RPA polarizability P^0 of equation (2.38). The kernel

$$\Xi(3,6;4,5) = i\,\frac{\delta[\,v_H(3)\,\delta(3,4) + \Sigma(3,4)\,]}{\delta G(5,6)} \quad (2.44)$$

links the non-interacting L_0 to the fully interacting L, just as the self-energy did for the single-particle Green function.
The kernel written above is formally exact but not directly usable, since it contains both the self-energy and its functional derivative. It is then approximated consistently with the GW self-energy. Inserting $\Sigma = iGW$, neglecting the derivative $\delta W/\delta G$ (hence keeping the screening constant), and treating W as static, the kernel splits into two contributions

$$\Xi = v - W. \quad (2.45)$$

The first term arises from the variation of the Hartree potential and is the bare repulsive electron-hole exchange, while the second comes from the variation of Σ and is the statically screened Coulomb attraction between the electron and the hole. In the RPA kernel, instead, only the Coulomb interaction is present, making the excitonic effects disappear. It is often convenient to turn this integral equation into an eigenvalue problem. Projecting onto the basis of single-particle transitions built from the mean-field orbitals, and diagonalizing L_0[26], the BSE is mapped onto an effective two-particle excitonic Hamiltonian. Denoting occupied orbitals by v, v' and empty ones by c, c', its resonant block reads, in the basis of the transitions from occupied to empty states,

$$A_{(vc)(v'c')} = \left(\varepsilon_c^{\mathrm{QP}} - \varepsilon_v^{\mathrm{QP}}\right) \delta_{vv'}\delta_{cc'} + 2\,\bar{v}_{(vc)(v'c')} - W_{(vc)(v'c')}, \tag{2.46}$$

where $\varepsilon^{\mathrm{QP}}$ are the GW quasiparticle energies. The two interaction matrix elements are

$$\bar{v}_{(vc)(v'c')} = \int dr\, dr'\; \phi_v^*(r)\, \phi_c(r)\; v(r,r')\; \phi_{v'}(r')\, \phi_{c'}^*(r'), \tag{2.47}$$

$$W_{(vc)(v'c')} = \int dr\, dr'\; \phi_v^*(r)\, \phi_{v'}(r)\; W(r,r';\omega=0)\; \phi_c(r')\, \phi_{c'}^*(r'), \tag{2.48}$$

v being the bare Coulomb interaction and W the statically screened one. The diagonal term maps each excitation onto the corresponding transition energy, while the interaction couples different transitions among themselves. In its most general form, the excitonic Hamiltonian also couples the resonant $v \to c$ transitions to the antiresonant ones, $c \to v$, through an off-diagonal block B that makes the problem non-Hermitian. The excitation energies Ω_s and the corresponding amplitudes (X^s, Y^s) then follow from the eigenvalue problem

$$\begin{pmatrix} A & B \\ B^\dagger & A^\dagger \end{pmatrix} \begin{pmatrix} X^s \\ Y^s \end{pmatrix} = \Omega_s \begin{pmatrix} 1 & 0 \\ 0 & -1 \end{pmatrix} \begin{pmatrix} X^s \\ Y^s \end{pmatrix}. \tag{2.49}$$

Neglecting the coupling block by setting $B = 0$ defines the Tamm-Dancoff approximation (TDA), in which the antiresonant part decouples as $Y^s = 0$, and one has to work with a smaller, Hermitian matrix that simplifies the eigenvalue problem. It is accurate when $|B|$ is small compared to the resonant transition energies[27]. Either way, each excitation is a coherent superposition of independent quasiparticle transitions, and it is this mixing that reshapes the absorption spectrum with respect to the RPA, shifting the excitation energies and redistributing the oscillator strength among the different transitions.

[26] This is done by retaining, for each state, only the quasiparticle pole at the GW energy $\varepsilon^{\mathrm{QP}}$ and discarding the satellite structures.

[27] In this thesis the full problem is solved, and the TDA is examined separately as one of the methodological tests of chapter 3.

2.6.2 Polarizability and photoabsorption cross section

The optical observables computed in this thesis are built from the neutral excitation energies Ω_s and the eigenvectors (X^s, Y^s).
The coupling of each excitation to an external electromagnetic field, within the dipole approximation, is measured by the *oscillator strength*, whose Cartesian component along the direction x is

$$f_s^x = \sum_{vc} \langle \phi_v | \hat{x} | \phi_c \rangle \left(X_{vc}^s + Y_{vc}^s \right), \tag{2.50}$$

where $\hat{x}$ is the position operator. X_{vc}^s and Y_{vc}^s are the components, in the space of the transitions, of the previously defined vectors X^s and Y^s - meaning that they are the weights of the resonant $(v \to c)$ and antiresonant $(c \to v)$ transitions in the s-excitation. These quantities determine the *dynamical dipole polarizability*, which measures the dipole induced on the electronic cloud by an oscillating field. Expanded over the excited states, it reads

$$\alpha_{xx'}(\omega) = \sum_s \frac{2\,\Omega_s\, f_s^x\, f_s^{x'}}{\Omega_s^2 - (\omega + i\eta)^2}, \tag{2.51}$$

with a pole at each excitation energy Ω_s. This means that the excitation energies fix the positions of the resonances, and the oscillator strengths govern their intensities. The quantity measured in an absorption experiment is the *photoabsorption cross section*, which is proportional to the imaginary part of the polarizability averaged over all molecular orientations $\bar{\alpha}(\omega) = \frac{1}{3} \sum_x \alpha_{xx}(\omega)$,

$$\sigma(\omega) = \frac{4\pi\omega}{c} \operatorname{Im} \bar{\alpha}(\omega), \tag{2.52}$$

so that the spectrum is a series of peaks at the excitation energies Ω_s, broadened by the finite η and with intensities set by the oscillator strengths. It is also possible to prove that the total oscillator strength obeys the Thomas-Reiche-Kuhn sum rule

$$\tfrac{2}{3} \sum_s \Omega_s \sum_x \left(f_s^x \right)^2 = N_{\text{el}},$$

N_{el} being the number of electrons. It holds exactly only in the limit of a complete basis set, and therefore provides a check for the basis-set convergence.

2.7 Computational details

All the electronic-structure and spectroscopy calculations presented in this work were performed using MOLGW [22], a many-body perturbation theory package for atoms, molecules, and clusters that implements the GW approximation and the Bethe-Salpeter equation on Gaussian basis sets. The molecular geometries were initially optimized with

NWChem [23] and compared with those reported in the NIST Chemistry WebBook [24] and in the NIST Computational Chemistry Comparison and Benchmark Database (CCCBDB) [25]. The optimized geometries were then used consistently throughout all the following calculations.

2.7.1 Gaussian basis sets and the RI approximation

The single-particle wave functions are expanded in a basis of Gaussian-type orbitals centred on the atomic nuclei. Each basis function is a *contracted Gaussian*, a fixed linear combination of primitive Gaussians of the form $e^{-\alpha|\mathbf{r}-\mathbf{R}_N|^2}$, where $\mathbf{R}_N$ is the position of nucleus N. Unlike plane waves, which are natural for periodic solids, Gaussian orbitals are localized around the atoms and their integrals can be evaluated analytically, making them computationally efficient for molecules. In this work, calculations are performed with the Dunning basis sets cc-pVTZ, aug-cc-pVTZ, aug-cc-pVQZ and aug-cc-pV5Z. The augmented (aug-) sets include diffuse functions that are important for the description of excited states and polarizability. A practical bottleneck in GW and BSE calculations is the evaluation of the four-centre Coulomb integrals $(ia|jb)$,[28] whose number grows rapidly with the basis-set size. MOLGW avoids this by using the resolution-of-the-identity (RI) approximation: the products of pairs of orbitals are expanded in an auxiliary basis, in order to replace the four-centre integrals with sums of products of two- and three-centre integrals, reducing the computational cost of the problem. Each orbital basis then has a matched auxiliary counterpart, denoted with the suffix `-RI`, which is specified in the input.

2.7.2 Workflow and computational settings

The calculations discussed in this thesis follow a three-step workflow. First, a self-consistent field calculation is performed within the Kohn-Sham theory to obtain the mean-field orbitals and eigenvalues. These are then used as the starting point for a G_0W_0 calculation, which corrects the Kohn-Sham eigenvalues into quasiparticle energies. Finally, the BSE is solved[29] to obtain the neutral excitation energies and the corresponding eigenvectors, from which the photoabsorption cross section and the dynamical dipole polarizability are computed.
There are many input parameters that govern the accuracy of the calculations. One can select the post-SCF method through the `postscf` input, and the parameter `nvirtualw`[30]

[28] This is a common notation for $\iint \phi_i^*(\mathbf{r}_1)\phi_a(\mathbf{r}_1)\,\frac{1}{|\mathbf{r}_1-\mathbf{r}_2|}\,\phi_j^*(\mathbf{r}_2)\phi_b(\mathbf{r}_2)\,\mathrm{d}\mathbf{r}_1\mathrm{d}\mathbf{r}_2$.

[29] While the BSE kernel relies on the GW approximation of the self-energy, a further approximation is often introduced in the diagonal block of the excitonic Hamiltonian, where the quasiparticle energies are not explicitly computed but approximated by applying a rigid shift of the Kohn-Sham eigenvalues that reproduces the GW gap. Both approaches are used in this thesis, as specified throughout chapter 3.

[30] From now on called n_{vw} for brevity.

specifies the first state beyond which virtual states are excluded from W and from the BSE calculation. It is thus possible to study the convergence of the spectrum as a function of n_{vw}, as both the GW self-energy and the BSE excitation energies depend on this truncation. The broadening parameter η, set to 0.01 eV in all calculations, controls the Lorentzian width of the peaks in the computed spectra and corresponds directly to the η of equation 2.51. The exchange-correlation functional used in the first generalised Kohn-Sham step is specified via `scf`. In this thesis the functionals PBE, PBE0 and BHLYP were used. In addition to the full BSE calculation, two further approximations are tested in this thesis: the already discussed TDA and the scissor approximation. In the latter, the quasiparticle corrections obtained from GW are approximated by applying a rigid shift to the Kohn-Sham eigenvalues.

2.7.3 Core-level spectra

The NEXAFS spectra are obtained by not *freezing* the core electrons in the BSE calculations, in order to include the transitions from the $1s$ core level alongside the valence ones. This is necessary to retain the core orbitals among the active occupied states, allowing transitions from the core level to be included in the excitation space. The setting `frozencore='no'` is therefore essential for core-level spectroscopy, while in valence BSE calculations the core electrons can, in principle, be frozen with little effect on the low-energy part of the spectrum.
In a standard MOLGW calculation, the frequency grid for the optical spectra and the number of printed excitations are truncated at values appropriate for valence excitations, which lie in the few-eV range. Since the core excitations considered in this thesis occur at much higher energies, the code has been modified in two points: the upper limit of the frequency grid was extended to cover the core-excitation region, and the number of printed eigenstates was increased so that the core-excitation region was adequately represented. This allows the analysis of the core-level part of the spectrum within the same BSE calculation that also contains the valence excitations.

Chapter 3

Results

In this chapter, the results obtained for H_2O, CH_4 and C_2H_4 are presented and discussed. First, the optimized molecular geometries are reported and compared with experimental values. The electronic structure is then analysed at the DFT and GW levels, focusing on the dependence of the single-particle energies, HOMO-LUMO gaps, and core-level binding energies on the exchange-correlation functional, basis set, and GW scheme employed. The discussion then turns to neutral excitations and photoabsorption spectra. Valence and core-level spectra are studied separately, assessing their convergence with respect to the basis set and the number of virtual states, as well as the effect of the quasiparticle starting point and of the Tamm-Dancoff and scissor approximations. Finally, the computed core-level excitation energies are compared with experimental and computational reference values.

3.1 Molecular geometries

The equilibrium geometries of H_2O, CH_4 and C_2H_4 were computed with NWChem using the Hartree-Fock method and two basis sets, 6-31G* and 6-31G**. The optimized bond lengths and angles are reported in table 3.1, together with experimental values from the NIST Computational Chemistry Comparison and Benchmark Database (CCCBDB). The computed geometries are in good agreement with experiment: bond lengths are underestimated by at most 0.023 Å, while the equilibrium angles agree to within 2° for all three molecules. Furthermore, the two basis sets give nearly identical results, indicating that the computed geometries are only weakly sensitive to the inclusion of the additional polarization functions. These geometries were then used as input for all subsequent MOLGW calculations, ensuring that the results are not affected by errors in the ground-state geometry.

Molecule	Parameter	HF/6-31G*	HF/6-31G**	Experiment
H_2O	r_{O-H} (Å)	0.947	0.943	0.958
	$\angle_{H-O-H}$ (°)	105.50	105.97	104.48
CH_4	r_{C-H} (Å)	1.084	1.084	1.087
	$\angle_{H-C-H}$ (°)	109.47	109.47	109.47
C_2H_4	$r_{C=C}$ (Å)	1.317	1.316	1.339
	r_{C-H} (Å)	1.076	1.076	1.086
	$\angle_{H-C-H}$ (°)	116.38	116.51	117.6
	$\angle_{H-C-C}$ (°)	121.81	121.74	121.2

Table 3.1: Equilibrium bond lengths and angles for H_2O, CH_4 and C_2H_4 computed with NWChem (HF/6-31G* and HF/6-31G**) and compared with experimental values.

3.2 Analysis of the electronic structure

The analysis of the electronic structure is organized in two steps. First, the Kohn-Sham eigenvalues and the density of states obtained from DFT are examined, as they provide a useful reference to assess the role of the basis set and the exchange-correlation functional on the single-particle spectrum. Then, the quasiparticle correction is applied to the Kohn-Sham eigenvalues within the GW approximation, hence restoring the physical meaning of the single-particle energies as addition and removal energies. The HOMO-LUMO gap and the core 1s binding energies are computed at the G_0W_0, G_nW_0 and G_nW_n levels, and their dependence on the basis set, the exchange-correlation functional and the main convergence parameters is discussed.

3.2.1 DFT Kohn-Sham eigenvalues and density of states

The density of states (DOS) provides a compact representation of the single-particle electronic structure, as it counts the number of available states per unit energy interval. Its features, such as the positions and widths of the peaks and the size of the gap between occupied and empty states, reflect the underlying orbital structure of the molecule, making it a useful quantity to analyse. Projecting the DOS onto angular-momentum channels (s, p, d) centered on each atom gives the *projected* density of states (PDOS), which allows one to identify the atomic and orbital character of each feature. The DOS and PDOS have here been used as a diagnostic tool. By examining how they change with respect to the basis set and the functional used to compute them, one can indeed assess whether the basis-set dependence of the optical spectra originates from the Kohn-Sham starting point, or rather from the construction of the screened interaction W or from the excitonic matrix.

To investigate the role of the exchange-correlation functional on the electronic structure, table 3.2 reports the HOMO-LUMO[1] gap computed for H_2O, CH_4, and C_2H_4 using different approximations. A trend emerges clearly from the data: the gap increases monotonically from PBE to PBE0 to BHLYP. This behaviour reflects the increasing fraction of exact exchange of the functional (see section 2.2.4): the exact-exchange contribution partly cancels the self-interaction error of the semi-local functional, which otherwise leaves the occupied levels too weakly bound, and it therefore lowers the HOMO, bringing it closer to the ionization potential. The virtual states are less sensitive to this correction, so that the LUMO increment is smaller. Therefore, the overall effect is a widening of the gap, mainly due to the lowering of the HOMO.

Molecule	Functional	cc-pVTZ	aug-cc-pVTZ
H_2O	PBE	6.933	6.272
	PBE0	9.807	8.703
	BHLYP	12.275	10.818
CH_4	PBE	10.261	9.078
	PBE0	12.564	11.026
	BHLYP	14.548	12.692
C_2H_4	PBE	5.769	5.658
	PBE0	7.997	7.790
	BHLYP	10.112	9.114

Table 3.2: HOMO-LUMO gap (eV) for H_2O, CH_4, and C_2H_4 as a function of the exchange-correlation functional for two basis sets.

However, the choice of the basis set plays an equally important role in determining the absolute values of these gaps. Table 3.3 shows the HOMO-LUMO gap, computed with the BHLYP functional, as a function of the basis set. The introduction of diffuse functions, passing from cc-pVTZ to aug-cc-pVTZ, reduces the gap for all molecules by approximately $1 - 2$ eV. This is physically expected, as diffuse functions are essential to describe accurately the long-range behaviour of the molecular orbitals[2]. Since the virtual states are more spatially extended than the occupied ones, they benefit from the addition of diffuse functions, which selectively stabilizes the LUMO and narrows the computed gap. Further enlargement of the basis set to aug-cc-pVQZ produces only a small change: the gap is essentially unchanged for CH_4 and C_2H_4 (the variation is below

[1]HOMO stands for Highest Occupied Molecular Orbital, LUMO for Lowest Unoccupied Molecular Orbital. In practice, the gap is calculated directly from the Kohn-Sham eigenvalues (ε_i) as $\Delta_{\mathrm{HL}} = \varepsilon_{\mathrm{LUMO}} - \varepsilon_{\mathrm{HOMO}}$.

[2]Hence, they describe better the asymptotic tails of the electron density.

0.04 eV), while H_2O undergoes a reduction of approximately 0.3 eV. This residual shift is nonetheless an order of magnitude smaller than the effect of adding the diffuse functions, and it decreases monotonically with the basis size. The main features of the basis-set dependence are thus already captured at the aug-cc-pVTZ level.

Molecule	cc-pVDZ	cc-pVTZ	aug-cc-pVTZ	aug-cc-pVQZ
H_2O	12.660	12.275	10.818	10.505
CH_4	15.440	14.548	12.692	12.663
C_2H_4	10.336	10.112	9.114	9.079

Table 3.3: HOMO-LUMO gap (eV) for BHLYP as a function of the basis set.

It is worth underlining that all DFT gaps reported here systematically underestimate the quasiparticle gap. This is a known DFT problem, which emerges as a consequence of the approximate treatment of exchange and correlation in the Kohn-Sham potential. The DOS and PDOS provide a more complete picture of the electronic structure.
The DOS is computed by broadening each Kohn-Sham eigenvalue with a Gaussian of width $\sigma = 0.5$ eV and plotting the result as a function of energy (relative to the HOMO). Two projection schemes are considered: *Löwdin* and *Mulliken*. While both are used here to decompose the total DOS into s, p, and d contributions, they differ in how contributions from a non-orthogonal basis are partitioned. The Mulliken scheme can yield non-physical results, particularly when diffuse basis functions are used, as their addition may lead to unpredictable changes in the resulting projections [26]. The Löwdin scheme instead performs the analysis in an orthogonalized basis and is more robust in this regime. For this reason, it is used here as the primary reference. However, the Mulliken result for H_2O is shown below for comparison.

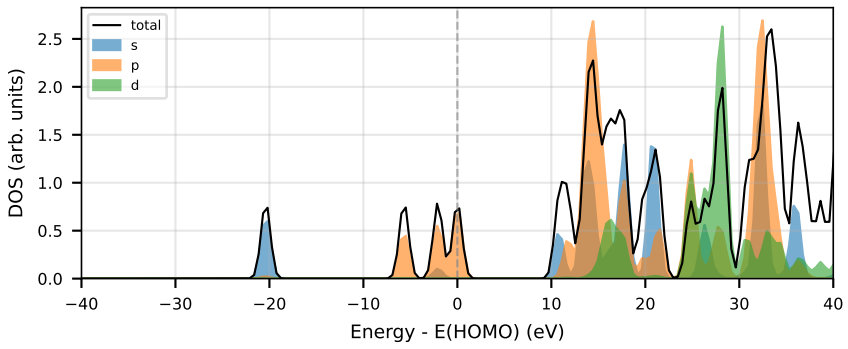

Figure 3.1: Mulliken projected density of states (PDOS) for H_2O computed with BHLYP and aug-cc-pVTZ in a restricted energy range. The projection is performed on the oxygen atom.

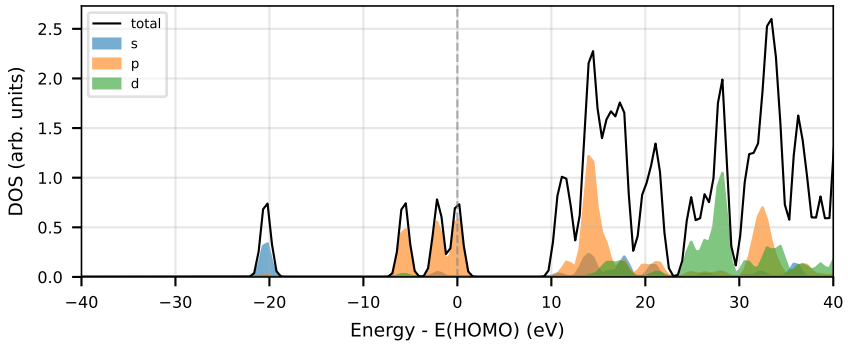

Figure 3.2: Löwdin projected density of states for H_2O computed with BHLYP and aug-cc-pVTZ in a restricted energy range. The projection is performed on the oxygen atom.

Figure 3.2 shows the Löwdin PDOS of H_2O computed with BHLYP and aug-cc-pVTZ, zoomed into the $[-40, 40]$ eV window around the HOMO, while figure 3.3 shows it in the full energy range. The occupied spectrum consists of two distinct regions: an isolated peak at approximately 20 eV below the HOMO, with predominantly s character, and a group of peaks in the $[-7, 0]$ eV range, with dominant p character. A clear gap separates the occupied from the virtual states, consistent with the HOMO-LUMO gap reported in table 3.2. In the full energy range, a further isolated peak appears at about 500 eV below the HOMO, with pure s character, corresponding to the oxygen 1s core level, which shows up in the projection because the core electrons are not frozen and the DOS is projected on the oxygen atom. Its Kohn-Sham position underestimates the experimental oxygen 1s binding energy, as discussed in section 3.2.3. The corresponding Mulliken PDOS is also shown: while the total DOS and the peak positions are identical, the projected weights differ substantially, with the p and d components of the virtual states being strongly overestimated, an artefact of the diffuse basis functions, as discussed above.

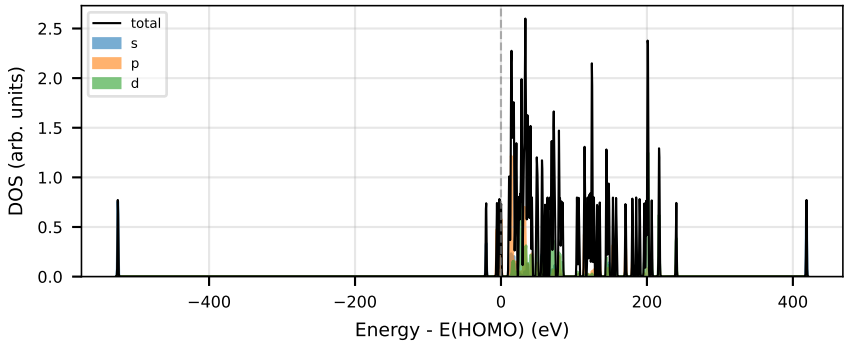

Figure 3.3: Löwdin projected density of states for H_2O computed with BHLYP and aug-cc-pVTZ. The projection is performed on the oxygen atom.

The DOS of CH_4 and C_2H_4 show the same qualitative structure, with an isolated C 2s peak at lower binding energy and a group of C 2p-derived valence peaks near the HOMO. For C_2H_4, the presence of a C=C double bond introduces additional splitting in the valence region, reflecting the separation between the σ and π orbitals.
A further analysis conducted on the previously discussed basis sets finally shows that the DOS is practically independent of them: the positions and relative intensities of the peaks change negligibly when going from cc-pVTZ to aug-cc-pVTZ to aug-cc-pVQZ.

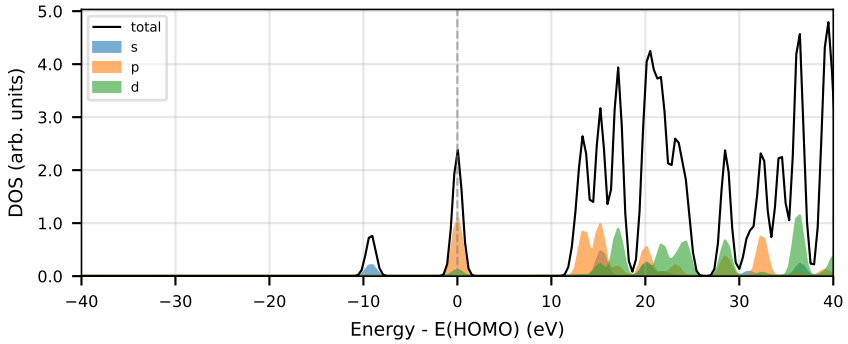

Figure 3.4: Löwdin projected density of states for CH_4 computed with BHLYP and aug-cc-pVTZ in a restricted energy range. The projection is performed on the carbon atom.

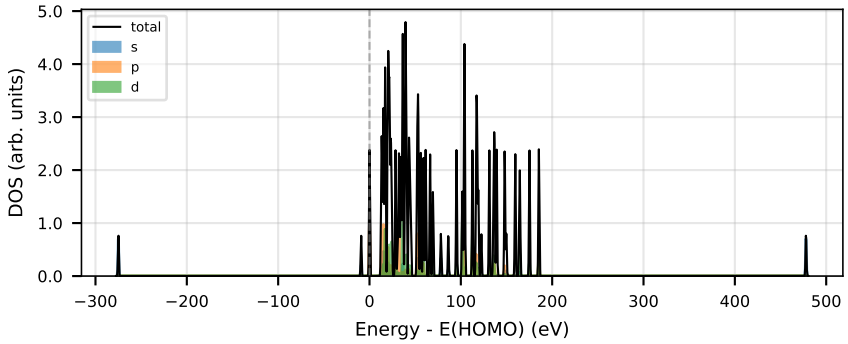

Figure 3.5: Löwdin projected density of states for CH_4 computed with BHLYP and aug-cc-pVTZ. The projection is performed on the carbon atom.

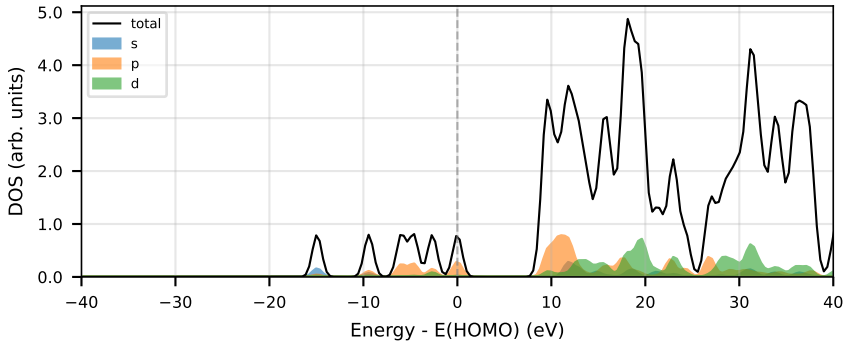

Figure 3.6: Löwdin projected density of states for C_2H_4 computed with BHLYP and aug-cc-pVTZ in a restricted energy range. The projection is performed on the carbon atom.

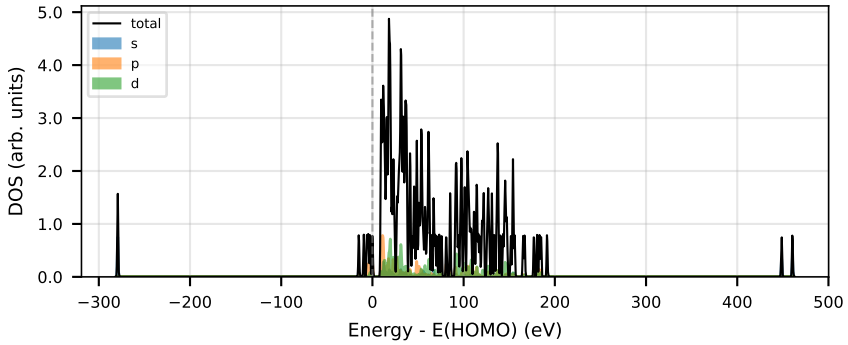

Figure 3.7: Löwdin projected density of states for C_2H_4 computed with BHLYP and aug-cc-pVTZ. The projection is performed on the carbon atom.

3.2.2 Quasiparticle energies: the GW approximation

As discussed in the previous chapter, the Kohn-Sham eigenvalues do not have a direct physical meaning, with the exception of the HOMO. Therefore, to obtain addition and removal energies to compare with the experimental ones, it is necessary to apply the GW approximation to the self-energy and compute the quasiparticle correction to the DFT results. Three levels of theory are considered here: G_0W_0, G_nW_0 and G_nW_n, already discussed in section 2.5.5. The resulting HOMO-LUMO gaps are collected in tables 3.4, 3.5 and 3.6. First, their dependence on the basis set and exchange-correlation functional was investigated, then an analysis of their convergence with respect to the main parameters used to compute them followed.

Molecule	Functional	cc-pVTZ	aug-cc-pVTZ	aug-cc-pVQZ	aug-cc-pV5Z
H_2O	PBE	15.180	12.658	12.772	12.805
	PBE0	15.519	12.986	13.119	13.149
	BHLYP	15.690	13.144	13.280	13.304
CH_4	PBE	17.128	14.801	14.855	14.864
	PBE0	17.492	14.996	15.042	15.043
	BHLYP	17.742	15.161	15.206	15.203
C_2H_4	PBE	12.681	12.110	12.119	12.122
	PBE0	13.015	12.417	12.431	12.433
	BHLYP	13.215	11.284	11.348	11.340

Table 3.4: HOMO-LUMO gap (eV) computed at the G_0W_0 level for H_2O, CH_4 and C_2H_4 as a function of the functional and the basis set.

The dominant basis-set effect is the addition of diffuse functions. Indeed, passing from cc-pVTZ to aug-cc-pVTZ diminishes the G_0W_0 gap by approximately 2.5 eV for both H_2O and CH_4, while for C_2H_4 the effect is smaller. Any further increase of the basis set dimension produces differences of the order of 0.1 eV, and hence converges more slowly than in the DFT calculations. This is due to the fact that the LUMO of H_2O and CH_4 is spatially extended: without adequate diffuse functions the basis confines it, overestimating its energy and consequently the gap too. In contrast, the augmented functions allow the orbital to relax to its actual spatial extent and correct energy. On the other hand, in C_2H_4 the π and π^* orbitals are more compact and hence less sensitive to diffuse functions. Augmented bases are thus essential already at the level of electronic structure, and aug-cc-pVTZ captures most of the basis-set effect on the gap. Because of the perturbative character of G_0W_0, the result also depends on the DFT starting point. For H_2O and CH_4 the gap increases with the fraction of exact exchange in the functional, reflecting the well-known starting-point dependence of the method. C_2H_4 appears to be an exception: with the augmented bases, BHLYP gives a noticeably smaller gap than PBE and PBE0, reversing the trend observed for the other two molecules. However, this apparent anomaly originates from the orbital-labelling convention adopted in table 3.4. The augmented bases provide a manifold of diffuse virtual states lying close to the valence π^* orbital. Since these states are nearly degenerate, their Kohn-Sham ordering is sensitive to the exchange-correlation functional, while the quasiparticle corrections are strongly state-dependent. In particular, π^* receives a larger quasiparticle correction than the diffuse states, so that the quasiparticle ordering may differ from the Kohn-Sham one: as a consequence, the state carrying the DFT LUMO index may not correspond to the lowest unoccupied quasiparticle state. The gaps reported in table 3.4 follow the DFT labelling. Such GW-induced orbital reordering has been discussed in [27].

Turning to the convergence parameters, the construction of W requires a sum over virtual states, whose number is controlled by n_{vw}. Figure 3.8 shows the convergence of the G_0W_0 gap as a function of n_{vw} for BHLYP and the two augmented bases. It is worth noting that the gap first decreases up to $n_{vw} \approx 30$ and then rises steadily. Within the range accessible with these bases, the curves do not reach a stationary point for either aug-cc-pVTZ or aug-cc-pVQZ. For H_2O/aug-cc-pVQZ, for instance, the gap still increases by about 0.15 eV between $n_{vw} = 130$ and $n_{vw} = 167$, with no sign of the increment decreasing. The slow convergence with respect to the number of virtual states is a limitation of GW with Gaussian bases. However, the residual variation is relatively small compared to the scale of the absolute gap. The same figures also report, with a star, the effect of freezing core states in the construction of W, controlled by the parameter n_{corew}. Freezing the $1s$ level ($n_{\text{corew}} = 1$), and for C_2H_4 also the two carbon $1s$ levels ($n_{\text{corew}} = 2$), changes the gap by less than 0.01 eV with respect to the original calculation, since the deep core states contribute negligibly to the screening at valence energies. This approximation is therefore justified and is used to reduce the cost of the more demanding calculations.

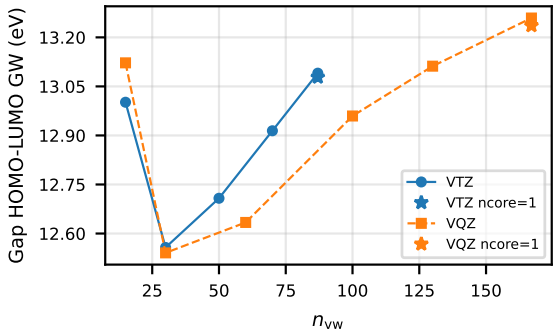

(a) H_2O

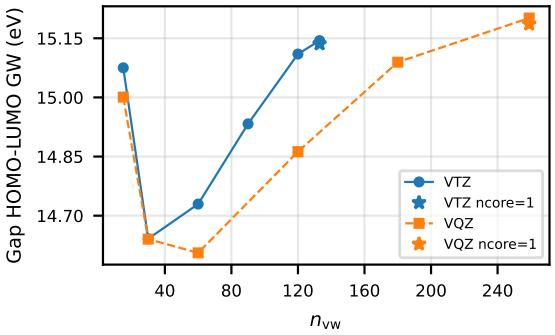

(b) CH_4

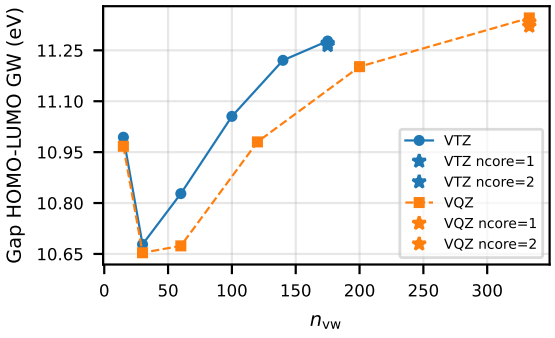

(c) C_2H_4

Figure 3.8: Convergence of the G_0W_0 HOMO-LUMO gap as a function of n_{vw} for H_2O, CH_4 and C_2H_4.

The role of self-consistency has also been studied. The gap increases systematically as one progresses from G_0W_0 to G_nW_0 to G_nW_n (tables 3.5 and 3.6), with a more pronounced effect for PBE than for BHLYP. Again, this highlights the starting-point dependence, as PBE begins from a strongly underestimated DFT gap, whereas BHLYP starts much closer to the self-consistent result and thus undergoes only minor corrections. As a consequence, the spread among different functionals is reduced at the G_nW_0 level. For instance, for H_2O with aug-cc-pVTZ as the basis set, the discrepancy among the three functionals falls from 0.49 eV at the G_0W_0 level down to just 0.17 eV. Self-consistency is iterated up to $n_{\text{step}} = 6$, but the gap is already stable at $n_{\text{step}} = 2$, confirming that G_0W_0 is a good starting point for BHLYP and that the partial and full self-consistent schemes only apply minor corrections. Figure 3.9 illustrates the convergence of the HOMO and LUMO energies for C_2H_4 with BHLYP as a representative case.

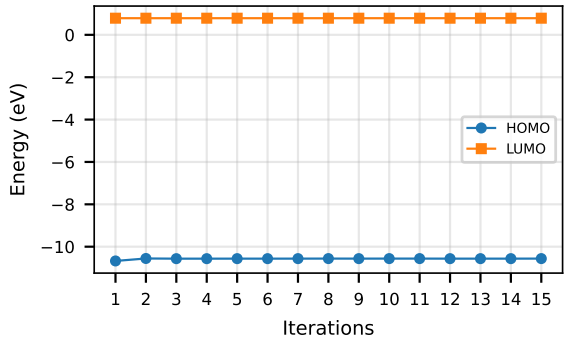

Figure 3.9: Convergence of the HOMO and LUMO energies as a function of the self-consistency iteration steps (n_{step}).

Molecule	Functional	cc-pVTZ	aug-cc-pVTZ	aug-cc-pVQZ	aug-cc-pV5Z
H_2O	PBE	15.727	13.418	13.614	13.677
	PBE0	15.780	13.327	13.489	13.540
	BHLYP	15.789	13.252	13.416	13.442
CH_4	PBE	17.610	15.289	15.367	15.386
	PBE0	17.736	15.227	15.295	15.298
	BHLYP	17.850	15.267	15.317	15.319
C_2H_4	PBE	13.031	12.530	12.542	12.547
	PBE0	13.188	12.604	12.622	12.625
	BHLYP	13.290	11.349	11.423	11.424

Table 3.5: HOMO-LUMO gap (eV) at the G_nW_0 level ($n_{\text{step}} = 6$).

Molecule	Functional	cc-pVTZ	aug-cc-pVTZ	aug-cc-pVQZ	aug-cc-pV5Z
H_2O	PBE	16.265	14.013	14.181	14.241
	PBE0	16.118	13.656	13.812	13.859
	BHLYP	15.971	13.422	13.576	13.610
CH_4	PBE	18.053	15.648	15.716	15.736
	PBE0	18.001	15.435	15.494	15.501
	BHLYP	17.999	15.375	15.431	15.429
C_2H_4	PBE	13.487	12.960	12.968	12.971
	PBE0	13.448	12.836	12.854	12.854
	BHLYP	13.422	11.416	11.493	11.492

Table 3.6: HOMO-LUMO gap (eV) at the G_nW_n level ($n_{\text{step}} = 6$).

The values reported in tables 3.4, 3.5 and 3.6 are computed with n_{vw} set to the full virtual space available for each basis, and are therefore to be read as the best estimate accessible with the given basis.
To complete the picture of the electronic structure, the DOS computed from the G_0W_0 quasiparticle energies is now compared with the Kohn-Sham one, described in the previous section. The quasiparticle DOS is obtained by broadening the G_0W_0 eigenvalues in the same way that was done for the DFT DOS (the same width was used and HOMO was set to zero). The comparison is shown in figure 3.10. The occupied states are essentially unchanged, while the virtual states are shifted towards positive energies by approximately 2.3 eV. This widens the gap from 10.8 eV at the Kohn-Sham level to 13.1 eV at the G_0W_0 level, in agreement with table 3.4. This means that the quasiparticle correction acts mainly on the empty states, leaving the occupied structure and the overall shape of the spectrum essentially unchanged.

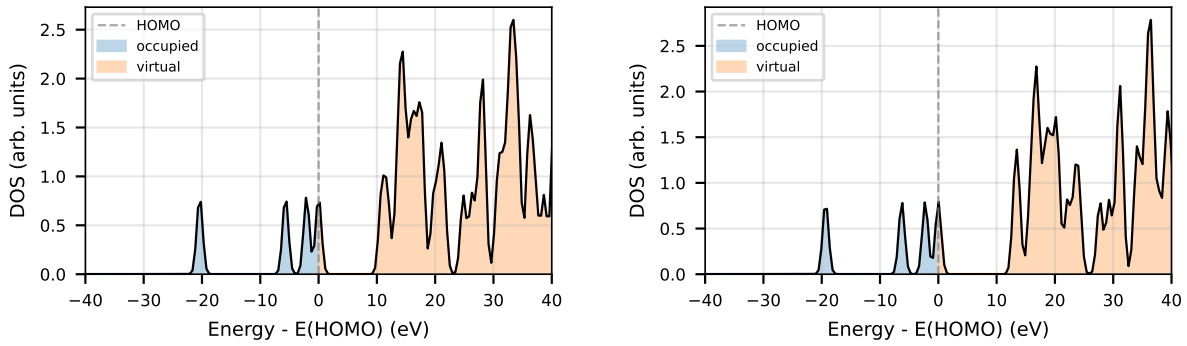

(a) DFT (Kohn-Sham) **(b)** G_0W_0

Figure 3.10: Density of states of H_2O computed with BHLYP and aug-cc-pVTZ with both the Kohn-Sham and the G_0W_0 methods.

For completeness, the DOS computed with G_nW_0 and G_nW_n is also shown below.

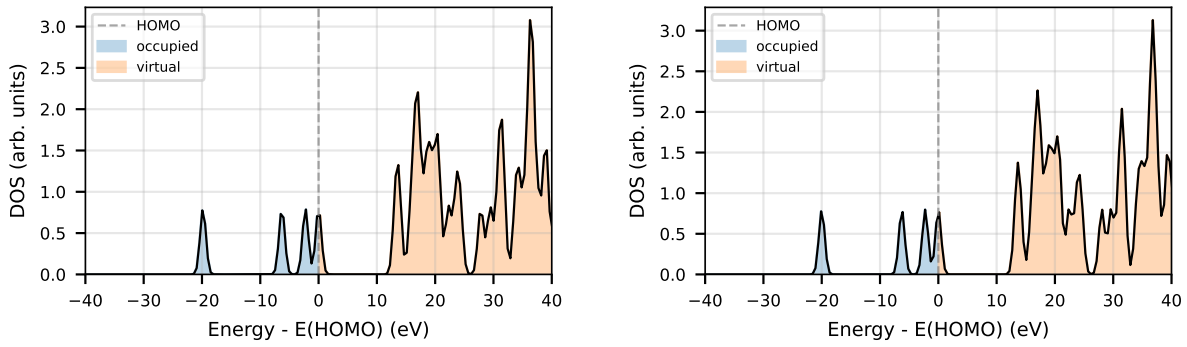

(a) G_nW_0 **(b)** G_nW_n

Figure 3.11: Density of states of H_2O computed with BHLYP and aug-cc-pVTZ with both the G_nW_0 and the G_nW_n methods.

3.2.3 Core-level binding energies

Finally, the $1s$ core-level binding energy has been computed at the DFT, G_0W_0, G_nW_0 and G_nW_n levels for the three molecules. The results are reported in table 3.7 as orbital energies[3].

[3]These energies are negative, since the state is bound.

Molecule	Functional	Basis	DFT	G_0W_0	G_nW_0	G_nW_n
H_2O	PBE	cc-pVTZ	−509.954	−538.682	−540.013	−540.879
		aug-cc-pVTZ	−510.527	−538.538	−536.331	−540.641
		aug-cc-pVQZ	−510.352	−538.714	−538.583	−540.758
		aug-cc-pV5Z	−510.382	−538.754	−538.771	−540.724
	PBE0	cc-pVTZ	−522.422	−539.755	−539.575	−541.153
		aug-cc-pVTZ	−522.893	−539.659	−539.488	−540.947
		aug-cc-pVQZ	−522.753	−539.857	−539.508	−541.118
		aug-cc-pV5Z	−522.764	−539.943	−540.428	−541.206
	BHLYP	cc-pVTZ	−535.402	−539.182	−540.294	−541.081
		aug-cc-pVTZ	−535.845	−539.112	−540.240	−540.936
		aug-cc-pVQZ	−535.728	−539.225	−540.447	−541.144
		aug-cc-pV5Z	−535.728	−539.205	−540.404	−541.221
CH_4	PBE	cc-pVTZ	−268.430	−289.947	−289.713	−291.649
		aug-cc-pVTZ	−268.437	−289.973	−289.692	−291.512
		aug-cc-pVQZ	−268.387	−290.221	−289.546	−291.640
		aug-cc-pV5Z	−268.397	−290.379	−289.765	−291.869
	PBE0	cc-pVTZ	−277.632	−290.954	−290.843	−292.108
		aug-cc-pVTZ	−277.634	−290.989	−290.875	−291.992
		aug-cc-pVQZ	−277.593	−291.375	−291.136	−292.663
		aug-cc-pV5Z	−277.594	−291.384	−291.266	−292.322
	BHLYP	cc-pVTZ	−287.420	−290.760	−291.674	−292.308
		aug-cc-pVTZ	−287.419	−290.779	−291.712	−292.253
		aug-cc-pVQZ	−287.385	−290.990	−292.003	−292.588
		aug-cc-pV5Z	−287.382	−291.086	−292.131	−292.646
C_2H_4	PBE	cc-pVTZ	−269.003	−290.081	−289.948	−291.878
		aug-cc-pVTZ	−269.060	−290.092	−289.791	−291.684
		aug-cc-pVQZ	−268.996	−290.391	−290.195	−291.898
		aug-cc-pV5Z	−269.015	−290.726	−290.507	−291.798
	PBE0	cc-pVTZ	−278.258	−291.170	−291.121	−292.258
		aug-cc-pVTZ	−278.306	−291.192	−291.094	−292.174
		aug-cc-pVQZ	−278.254	−291.488	−291.522	−292.435
		aug-cc-pV5Z	−278.260	−291.610	−291.513	−293.149
	BHLYP	cc-pVTZ	−288.032	−290.995	−291.910	−292.514
		aug-cc-pVTZ	−288.087	−290.999	−291.942	−292.475
		aug-cc-pVQZ	−288.043	−291.172	−292.119	−292.765
		aug-cc-pV5Z	−288.044	−291.318	−292.373	−293.059

Table 3.7: 1s core-level energy ε_{1s} (eV) for H_2O (O 1s), CH_4 (C 1s) and C_2H_4 (C 1s) computed with DFT, G_0W_0, G_nW_0 and G_nW_n ($n_{\text{step}} = 6$).

First, it is evident that DFT alone is not an adequate method for core levels. Not only is there a significant difference between the experimental results and the DFT calculations[4], but the latter is very sensitive to the functional. Indeed, for the O $1s$ of H_2O the energy ranges from -510 eV (PBE) to -536 eV (BHLYP), a spread of more than 25 eV. Adding the GW self-energy corrects this almost entirely: at the G_0W_0 level the O $1s$ energy of H_2O is ≈ -539 eV for all three functionals, hence removing most of the functional dependence and bringing the values close to the experimental binding energy. This is the central result of this section. Going beyond G_0W_0 with eigenvalue self-consistency (G_nW_0 and G_nW_n) modifies the core energy by approximately 1 to 2 eV. For these core levels the additional self-consistency does not improve the agreement with experiment: for H_2O, for instance, G_0W_0/BHLYP/aug-cc-pVTZ gives 539.1 eV against the experimental 539.7 eV, while G_nW_n gives 540.9 eV. Therefore, the G_0W_0 scheme on the BHLYP starting point is the best compromise for the core binding energies studied here. Furthermore, it is worth noting that the value for H_2O computed with G_nW_0, PBE and aug-cc-pVTZ is an outlier, as it differs by more than 2 eV from the other entries. This reflects a poorly converged self-consistent cycle for that specific starting point. Table 3.8 summarizes the comparison with experiment, taking G_0W_0/BHLYP/aug-cc-pVTZ as the reference value for this thesis. For all three molecules the computed binding energies fall within 0.6 eV of the measured ones, and within 0.2 eV for the two carbon $1s$ energies, in good agreement both with experiment and with other GW calculations.

Molecule	Experiment	Other GW work	This thesis
H_2O	539.7	539.08	539.112
CH_4	290.84	290.80	290.779
C_2H_4	290.82	290.87	290.990

Table 3.8: Absolute values of the $1s$ core binding energies. The computational and experimental values are from [28, 29].

These results are furthermore consistent with [30], where other schemes of comparable accuracy have been used.

3.3 Valence optical spectra

While the previous section dealt with charged excitations, the attention is now turned to neutral excitations. This is the regime in which the optical response of a system lies, as a promoted electron leaves a hole behind, and this effect is captured by the Bethe-Salpeter equation.

[4]The experimental results are shown in table 3.8.

This section analyses how the computed valence spectra depend on the main inputs of the calculation. First, the effect of the exchange-correlation functional is discussed, followed by the convergence with respect to the basis set and the number of virtual states. Finally, the role of the quasiparticle starting point and of the TDA and scissor approximation is assessed.

3.3.1 Effect of the exchange-correlation functional

Before turning to the convergence of the spectra with respect to the main computational parameters, it is useful to look at the role of the exchange-correlation functional used as a starting point for the optical spectra. As already discussed, the functionals PBE, PBE0 and BHLYP differ in the fraction of exact exchange they include, and this is noticeable when one looks at the optical spectra.
The main effect of increasing the fraction of exact exchange is a shift of the whole photoabsorption[5] spectrum towards higher energies. Such behaviour reflects the underlying change in the DFT starting point; in particular, since the excitonic Hamiltonian is built from single-particle energies and orbitals, a larger gap raises the energy threshold for excitations, and the absorption bands move accordingly. This effect is consistent across the three molecules studied and preserves the overall structure of the spectrum, apart from a slight change in the peak intensity[6]. This shift therefore arises directly from the choice of the mean-field starting point rather than from the two-particle interaction terms of the excitonic Hamiltonian. Given that the Kohn-Sham eigenvalues lack a direct physical meaning, the absolute position of these peaks cannot indicate which functional is more accurate: a physically meaningful prediction of the excitation energies hence requires the inclusion of quasiparticle corrections. For this reason, and since BHLYP represents the most suitable starting point for these corrections, the following analyses are carried out exclusively using the BHLYP functional.

3.3.2 Effect of the basis set

Now the convergence of the valence optical spectra with respect to n_{vw} and the one-particle basis set is analysed. As previously mentioned, all calculations in this section are performed using the BHLYP functional, which is the reference functional adopted throughout this work.
All the optical spectra in this section are computed within the RPA@DFT approximation: in terms of the excitonic Hamiltonian, this means that the attractive term $-W$ is omitted, so that its resonant block now reads

$$A^{\mathrm{RPA}}_{(vc)(v'c')} = (\varepsilon_c - \varepsilon_v)\,\delta_{vv'}\delta_{cc'} + 2\,\bar{v}_{(vc)(v'c')}.$$

[5]This is true for both the photoabsorption cross section and the dynamical dipole polarizability.
[6]The peak intensity grows as the exact exchange fraction increases.

The results of this omission are visible in table 3.9, as the first optically active transition lies slightly above the HOMO-LUMO gap (with aug-cc-pVTZ there is a blue shift of less than 0.2 eV, as can be seen from table 3.3), with no excitonic binding. This is what is expected when W is neglected, since v is repulsive and does not bind the electron-hole pair. Therefore, the following analysis characterises the basis-set convergence of the transition energies within this well-defined approximation[7].
First, the convergence of the spectrum with respect to n_{vw}, with a fixed basis set, is studied. To this end, the photoabsorption spectrum was computed for each basis using increasing values of n_{vw}, up to the maximum number of states available in that basis. Then, to illustrate the convergence behaviour, the difference $\Delta\sigma(\omega) = \sigma_{n_{vw}}(\omega) - \sigma_{\max}(\omega)$ has been plotted, representing the variation of the photoabsorption cross section $\sigma(\omega)$ as n_{vw} increases. Figure 3.12 shows the H_2O/aug-cc-pV5Z representative case: the difference is large for small n_{vw}, but decreases monotonically, becoming negligible over the whole energy range well before the maximum is reached. The same behaviour is found for all molecules and all basis sets. This confirms that, for each basis, the spectrum converges in n_{vw}, meaning that any residual dependence on the basis set cannot be attributed to an incomplete summation over the virtual states.

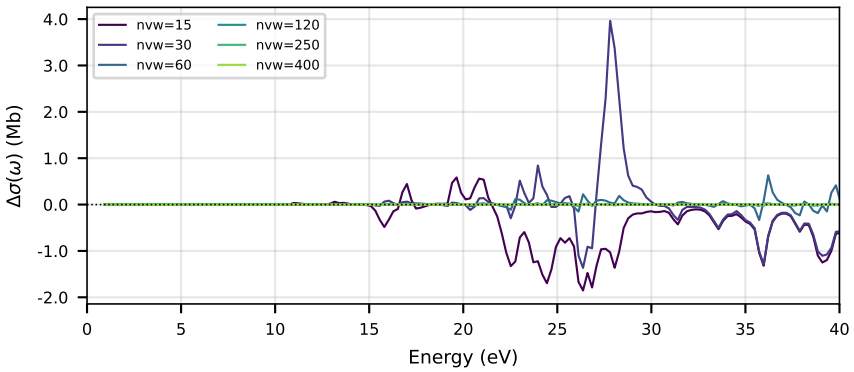

Figure 3.12: Convergence of the H_2O photoabsorption spectrum with respect to the number of virtual states n_{vw}, for the aug-cc-pV5Z basis set.

Having established convergence in n_{vw}, the dependence on the basis set can be analysed without ambiguity. Figures 3.13, 3.14 and 3.15 compare the spectra obtained with aug-cc-pVTZ, aug-cc-pVQZ and aug-cc-pV5Z, each computed with n_{vw} at its maximum. It is useful to distinguish two regions. Below approximately 13 eV [8], the three bases are in good agreement: the onset and the first peaks fall at nearly the same energies with similar intensities. At higher energies, on the other hand, the spectra diverge: peak

[7]The effect of switching on W is discussed in section 3.3.3.

[8]This is just above the ionization energy of the three molecules, which is approximately 10.5 eV for C_2H_4 and 12.6 eV for H_2O and CH_4 according to [24].

positions and intensities differ substantially between the three bases, and increasing the basis size does not improve the convergence. Such behaviour is in contrast to what was observed for the HOMO-LUMO gap, which converged smoothly once diffuse functions were included.

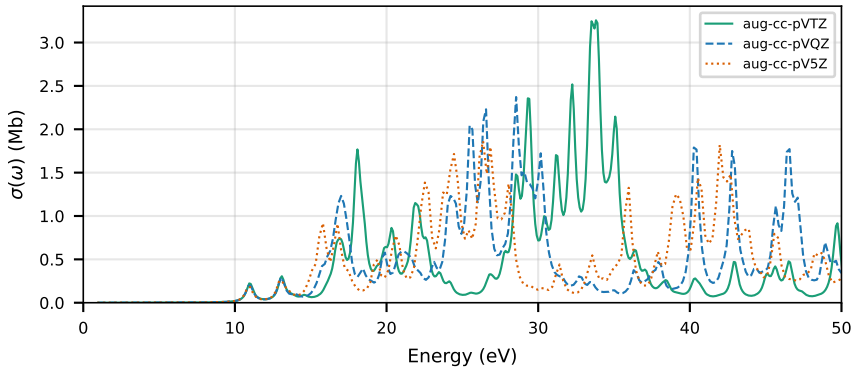

Figure 3.13: Photoabsorption spectra of H_2O computed with the three augmented bases.

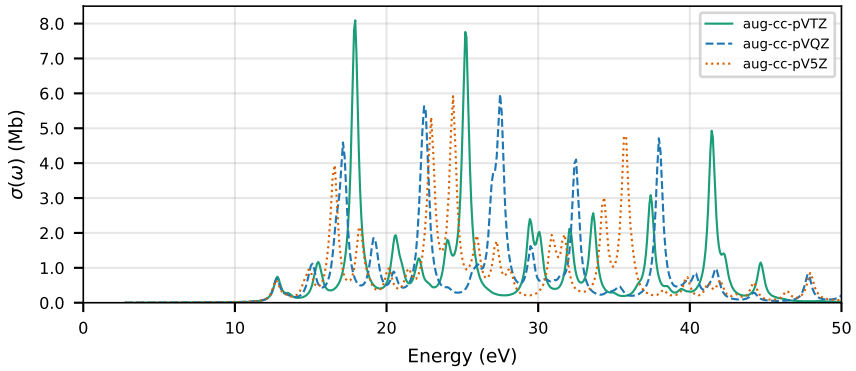

Figure 3.14: Photoabsorption spectra of CH_4 computed with the three augmented bases.

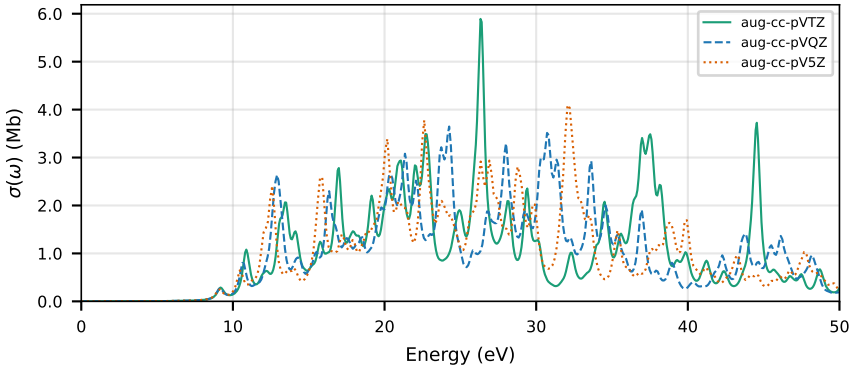

Figure 3.15: Photoabsorption spectrum of C_2H_4 computed with the three augmented bases.

The origin of this behaviour becomes clear when one investigates individual transitions rather than the whole spectrum. The lowest excitations, corresponding to transitions towards bound states localized around the molecule, are well described by all three bases. Table 3.9 reports the energy of the first excitation for each molecule: the three bases agree to within 0.1 eV, so these excitations can be considered converged with respect to the basis. The same good basis-set convergence of the bound optical excitations was reported in [22].

Molecule	aug-cc-pVTZ	aug-cc-pVQZ	aug-cc-pV5Z
H_2O	10.979	10.959	10.922
CH_4	12.792	12.755	12.721
C_2H_4	9.179	9.140	9.099

Table 3.9: Energy (eV) of the first optically active excitation, computed within the RPA@DFT approximation with the three augmented bases.

At higher energies, the situation is completely different. Above the ionization threshold, the final state belongs to the continuum of states in which the excited electron is unbound. Such a state is spatially extended and does not decay to zero away from the molecule, and hence it cannot be described by a finite linear combination of localized Gaussian functions. Therefore, the calculation cannot reproduce the continuum, and returns a finite set of discrete L^2 states, whose number and energies depend on the basis, so that changing the basis yields a different result[9]. The same basis dependence of unbound states is documented in the literature: in GW calculations on small molecules, quasiparticle states above the vacuum level differ strongly between Gaussian and plane-wave results, in contrast with the close agreement found for bound states [31].

[9]This is mainly due to the fact that the oscillator strength is redistributed in a different way.

Finally, a manifestation of the proliferation of diffuse functions in larger basis sets is the onset of numerical linear dependence. As the number of diffuse functions increases, some become nearly a linear combination of the others, and the overlap matrix becomes almost singular: this phenomenon is called *overcompleteness*. MOLGW removes the redundant functions before the calculation, so that the effective number of virtual states is slightly smaller than the nominal one. This has been taken into account by always using the full available virtual space, as determined by the code after the filtering.

3.3.3 Starting point and methodological approximations

The spectra discussed so far were computed within the RPA@DFT approximation, omitting the screened electron-hole interaction term and using the Kohn-Sham eigenvalues. However, a quantitative description of the excitation energies requires quasiparticle corrections. In this section the full BSE, including the screened electron-hole interaction previously neglected, is solved on top of the G_nW_0 quasiparticle energies (BSE@G_nW_0), and compared with the TDA and scissor approximation.
The impact of the electron-hole interaction is already evident from the lowest excitation. For instance, for H_2O the first optically active transition moves from 10.98 eV, computed within the RPA@DFT approximation, to 6.89 eV at the full BSE@G_nW_0 level. This large variation cannot be attributed to the difference in the starting point alone: the G_nW_0 correction opens the quasiparticle gap and, by itself, would push the spectrum towards higher energies. The fact that the transition moves, instead, to a lower energy shows that the attractive term $-W$, when switched on, dominates over the GW correction, reversing the sign of the overall deviation. Therefore, the excitonic effects are essential to provide an appropriate description of neutral excitations. In what follows, BSE@G_nW_0 is used as reference.
Figures 3.16, 3.17 and 3.18 show the photoabsorption cross section computed with these schemes for the three molecules. They show that the TDA reproduces the full BSE result very closely, as the peak positions are essentially unchanged and the only appreciable difference is an overestimation of their intensities. This confirms that the TDA is an accurate alternative to the full BSE calculation for finite systems, as the coupling it neglects is actually small.

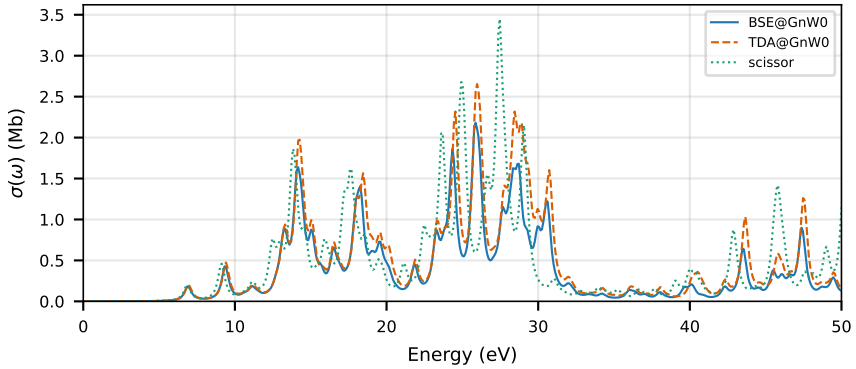

Figure 3.16: Photoabsorption spectra of H_2O obtained with BSE@G_nW_0, TDA and the scissor approximation.

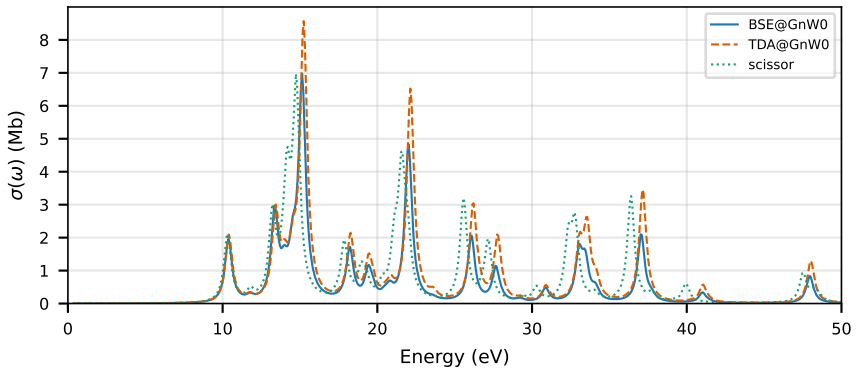

Figure 3.17: Photoabsorption spectra of CH_4 obtained with BSE@G_nW_0, TDA and the scissor approximation.

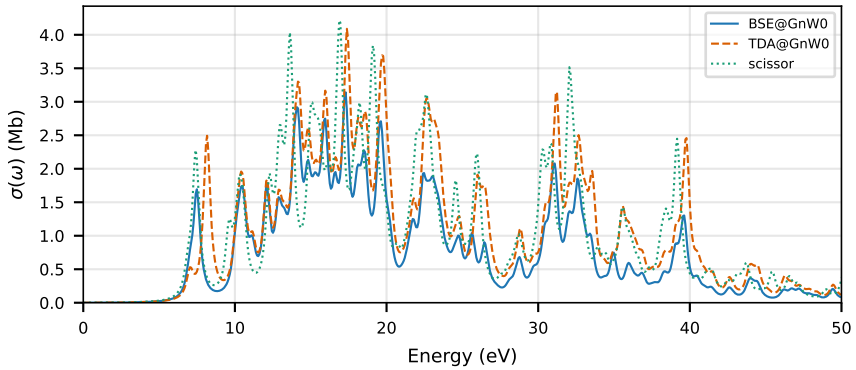

Figure 3.18: Photoabsorption spectra of C_2H_4 obtained with BSE@G_nW_0, TDA and the scissor approximation.

Furthermore, the scissor approximation[10] accurately reproduces the BSE@G_nW_0 results only within the low-energy region, near the optical threshold, where the rigid shift is sufficient to place the first transitions correctly. On the other hand, at higher energies the scissor spectrum progressively departs from the reference: peak positions are shifted and intensities are redistributed incorrectly. This is an expected failure, as the scissor assumes that the quasiparticle correction is a rigid shift, while the G_nW_0 correction depends on the state. Therefore, such an approximation cannot reproduce the correct positions and spacing of the higher transitions.

3.4 Core-level spectra

This section focuses on the core-level photoabsorption spectra of the three molecules. First, the convergence with respect to the number of virtual states and the basis set is investigated. The influence of the quasiparticle starting point is then assessed, together with the accuracy of the Tamm-Dancoff and scissor approximations. Finally, the computed K-edge transition energies are compared with experimental values and with results from previous GW-BSE calculations.

3.4.1 Convergence in n_{vw}

First, the convergence of NEXAFS spectra with respect to n_{vw} is studied. This is done in the same way as in section 3.3.2, by investigating the difference $\Delta\sigma(\omega) = \sigma_{n_{vw}}(\omega) - \sigma_{\max}(\omega)$ between the spectrum computed with a given n_{vw} and the one obtained using the full virtual space. Figure 3.19 shows H_2O/aug-cc-pVQZ as a representative case.

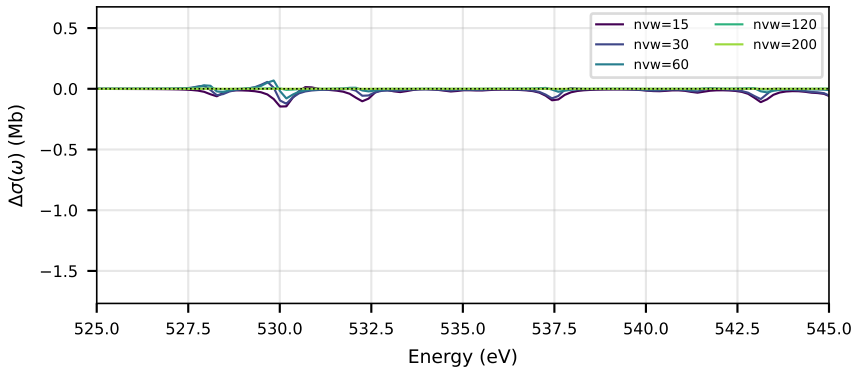

Figure 3.19: Convergence of the H_2O NEXAFS spectrum with respect to the number of virtual states n_{vw}, for the aug-cc-pVQZ basis.

[10]The shift was chosen as the difference between the G_nW_0 and DFT HOMO-LUMO gaps.

The convergence is rapid and smoother than for the valence spectra. The difference is small even for low values of n_{vw} and becomes negligible over the near-edge region as n_{vw} increases. Indeed, the residual variation is of the order of 0.1 Mb[11]. Such behaviour can be explained by the fact that these excitations start from a compact $1s$ orbital and reach localized bound states, therefore a limited number of virtual states is needed to model the screening and the excitonic Hamiltonian. It is also worth noting that the position of the K-edge is particularly stable.

3.4.2 Effect of the basis set

Now the dependence of the NEXAFS spectra on the basis set is investigated, comparing the three bases aug-cc-pVTZ, aug-cc-pVQZ and aug-cc-pV5Z. Figures 3.20, 3.21 and 3.22 show the near-edge region for the three molecules. As for the valence spectra (section 3.3.2), it is useful to distinguish two different regions.
In the lower energy region, close to the absorption threshold, the three augmented bases are in excellent agreement, as both the position and intensity of the first peaks coincide almost perfectly. This is particularly true for the first bound core resonance, whose position is essentially independent of the basis. This is the most physically relevant part of the spectrum, as it represents the transitions from the $1s$ level to localized bound states, which can be described properly by a Gaussian basis.

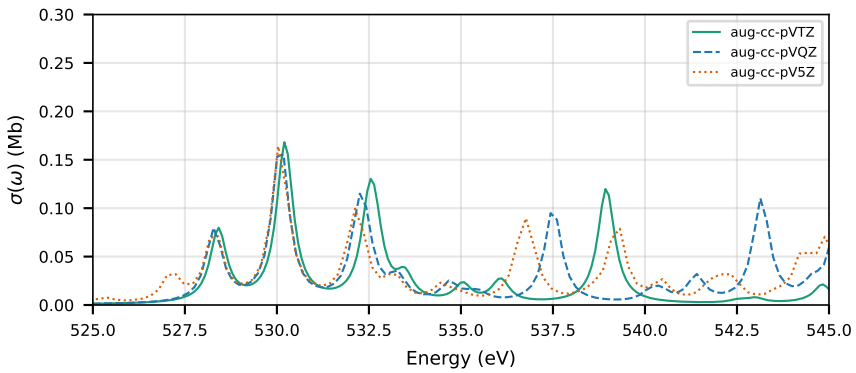

Figure 3.20: NEXAFS spectrum of H_2O computed with the three augmented bases.

[11] $1\text{Mb} = 10^{-18}\text{cm}^2$.

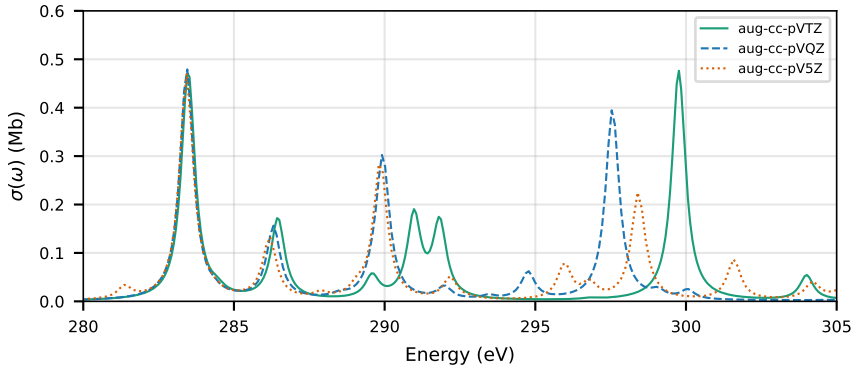

Figure 3.21: NEXAFS spectrum of CH_4 computed with the three augmented bases.

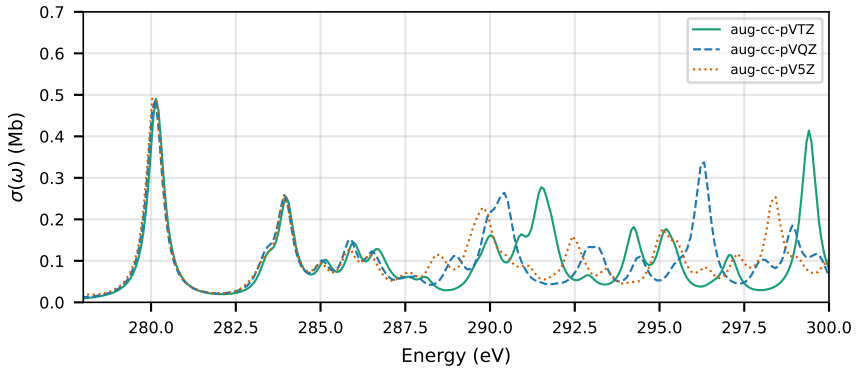

Figure 3.22: NEXAFS spectrum of C_2H_4 computed with the three augmented bases.

On the other hand, at higher energies, the spectra diverge: above roughly 535 eV for H_2O and 290 eV for CH_4 and C_2H_4, the peak positions and intensities change substantially among the three basis sets. The same behaviour was observed for the valence spectra: above the ionization threshold the final states belong to the continuum, which a finite localized Gaussian basis cannot represent. Only the bound resonances are therefore converged with respect to the basis.

3.4.3 Starting point and methodological approximations

As for the valence spectra (section 3.3.3), the impact of the starting point and of the TDA and scissor approximation[12] is now assessed for the NEXAFS spectra. Figure 3.23 compares the three schemes for the three molecules, and two clear trends emerge.

[12]The shift has been set equal to the G_nW_0 correction of the $1s$ level.

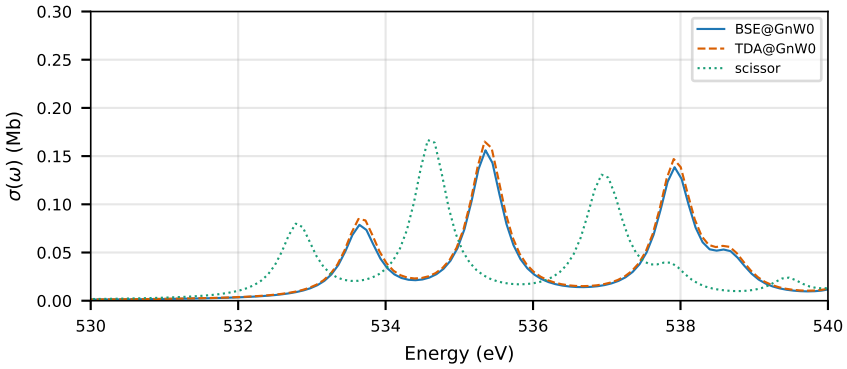

Figure 3.23: NEXAFS spectra of H_2O obtained with BSE@G_nW_0, TDA and the scissor approximation.

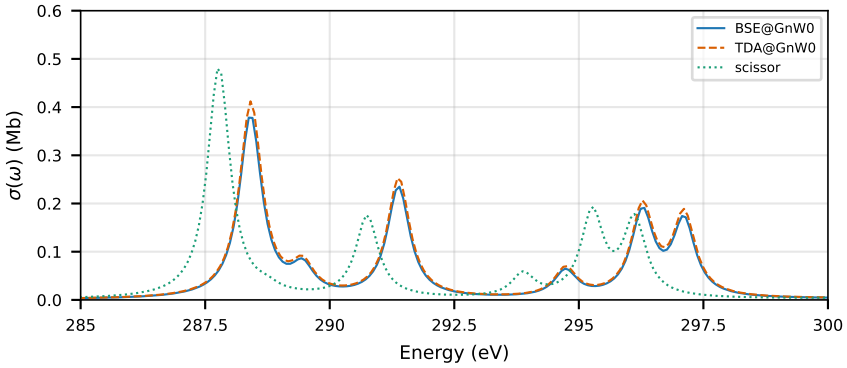

Figure 3.24: NEXAFS spectra of CH_4 obtained with BSE@G_nW_0, TDA and the scissor approximation.

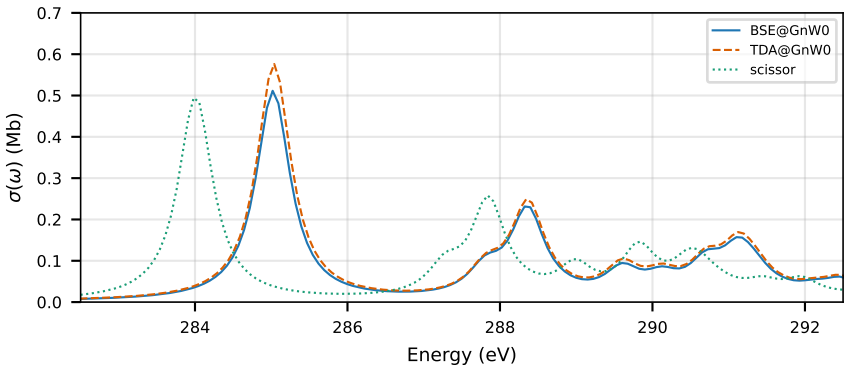

Figure 3.25: NEXAFS spectra of C_2H_4 obtained with BSE@G_nW_0, TDA and the scissor approximation.

First, the TDA reproduces the full BSE results almost exactly, as the peak positions and intensities coincide over the whole near-edge region. Furthermore, the K-edge onset agrees between the two methods to within 0.01 eV. This confirms that, for these finite systems, the Tamm-Dancoff approximation is an accurate and computationally cheaper alternative to the full BSE for core excitations too.
Second, the scissor approximation underestimates the transition energies. The rigid shift places the K-edge systematically below the BSE@G_nW_0 result: as reported in table 3.10, the first scissor peak lies between 0.6 and 1 eV lower than the BSE@G_nW_0 one for all three molecules. This phenomenon stems directly from the way the two schemes act on the single-particle energies: while the scissor raises all the virtual states by the same amount, the G_nW_0 correction is state-dependent and shifts the $1s$ level and each virtual state by a different amount. Therefore, the energy of a core transition is corrected by G_nW_0 through the combined shift of the initial and final states, whereas the scissor only displaces the virtual states by a single value. Furthermore, the underestimation is found to increase across the near-edge region, from about 0.86 eV at the K-edge to about 1.1 eV at $\simeq 10$ eV above it for H_2O.
This confirms that a quasiparticle starting point is essential for a quantitative description of the core spectra, and that its effect cannot be captured by a single rigid shift.

Molecule	BSE@G_nW_0	scissor	difference
H_2O	533.66	532.81	0.85
CH_4	288.41	287.77	0.64
C_2H_4	285.02	284.01	1.01

Table 3.10: Energy (eV) of the K-edge computed with BSE@G_nW_0, the scissor approximation and their difference.

3.4.4 Comparison with other results

Now, the K-edge transition energies obtained with the BSE@G_nW_0 scheme are compared with reference experimental values and selected computational ones. This comparison focuses on the position of the first dipole-allowed transition, namely the first transition carrying an appreciable oscillator strength in the purely electronic spectrum. For each molecule, this state is identified from the BSE eigenvalues and oscillator strengths. Table 3.11 summarizes the comparison with experiment. The deviations remain within approximately 0.4 eV for all three molecules, but the sign of the deviation depends on the system. For the oxygen K-edge of water, the transition energy is slightly underestimated (-0.34 eV), whereas the carbon transitions in methane and ethylene are slightly overestimated ($+0.41$ and $+0.35$ eV, respectively).
The BSE@G_nW_0 calculations do not include relativistic effects, which have been com-

Molecule	BSE@G_nW_0	Relativistic value	Experimental value
H_2O	533.66	534.08	534.0
CH_4	288.41	288.53	288.00
C_2H_4	285.02	285.14	284.67

Table 3.11: Energy (eV) of the first K-edge transition calculated with BSE@G_nW_0, its relativistic correction, and the experimental value. Experimental data: H_2O from [32]; CH_4 and C_2H_4 from [33].

puted in [34] on the $1s$ core level. This correction increases the transition energy by 0.42 eV for oxygen and 0.12 eV for carbon, consistent with the larger atomic number of oxygen. After applying this correction, the water transition energy shifts to 534.08 eV, in nearly exact agreement with experiment. On the other hand, the correction worsens the agreement for CH_4 and C_2H_4. This indicates that the residual energy difference is not primarily of relativistic origin. A further comparison can be made with the all-electron BSE@GW results reported in [32]. Their calculations were performed at the BSE@G_0W_0 level using the PBEh functional, with $\alpha = 0.45$, and their final setup included relativistic effects and carefully converged basis sets. For H_2O they obtain a K-edge transition energy of 532.74 eV, lower than the value obtained with the present BSE@G_nW_0 calculations. A similar difference in trend is found for C_2H_4: the authors of [32] report an underestimation of the carbon K-edge transition, whereas the present calculation slightly overestimates its experimental value. However, these differences should be interpreted with caution, since the two calculations employ different GW schemes and computational setups. Moreover, different experimental reference values are adopted for C_2H_4: [32] use 284.87 eV, whereas the value adopted here from [33] is 284.67 eV.
It is also worth discussing the CH_4 situation. This molecule does not have low-energy valence antibonding orbitals, as its lowest unoccupied states are spatially diffuse. The lowest-energy transition, forbidden by the dipole selection rules, is placed by the calculations at 287.07 eV[13], in great agreement with its experimental value, 287.05 eV [33]. Now, given that this transition carries no intensity, the first appreciable peak is the transition at 288.41 eV, whose experimental value is 288.00 eV. Furthermore, it is worth observing that the calculation correctly reproduces the ordering and markedly different intensities of these two low-lying states. At a purely electronic level, the lowest transition is dipole forbidden, whereas the following one carries a significant oscillator strength. While experimentally the latter gives rise to the first peak, the former can acquire a sizeable experimental intensity through vibronic coupling, which relaxes the selection rules. Therefore, the agreement extends beyond the energies themselves, as the calculation correctly describes also the dipole-forbidden character of the lowest state and the strong intensity of the following transition.

[13]This transition has been identified through its vanishing oscillator strength.

Chapter 4

Conclusions

This thesis aims to assess the reliability and accuracy of some computational choices and approximations involved in computing valence and core-level photoabsorption spectra within many-body perturbation theory, focusing on the GW approximation and the Bethe-Salpeter equation.
Since the analysed molecules, H_2O, CH_4 and C_2H_4, are already well characterised, the purpose of this work is not their description but rather the identification, through convergence tests and comparison with reference data, of a reliable and transferable scheme applicable to larger and less accessible systems. First, it is shown that the geometries obtained with the Hartree-Fock method closely reproduce the experimental structures, ensuring that the ground-state geometry is not a source of error in the following calculations.
The analysis of the electronic structure at the single-particle level demonstrates that the Kohn-Sham HOMO-LUMO gap grows with the fraction of exact exchange included in the functional, and is reduced by 1 to 2 eV when diffuse functions are added to the basis set. The gap is shown to have essentially reached convergence already at the aug-cc-pVTZ level, and it systematically underestimates the quasiparticle gap. The GW correction restores the physical meaning of the single-particle energies and acts almost exclusively on the empty states, leaving the occupied orbital structure essentially unchanged. Its magnitude depends strongly on the DFT starting point and, to a lesser extent, on the basis set, whose greatest effect occurs when transitioning from cc-pVTZ to the augmented bases. BHLYP proves to be the most convenient starting point, as it begins closer to the self-consistent result: eigenvalue self-consistency only slightly increases the gap and reduces the spread among functionals, with the gap being already stable after two iterations. Freezing the core states when constructing W changes the gap by less than 0.01 eV, and hence is a justified way to reduce the cost of more demanding calculations. The only actual limitation is the slow convergence of the GW gap with respect to n_{vw}, though the residual variations remain small compared to the gap itself. For the core levels, DFT alone is inadequate - the O $1s$ energy of H_2O differs by more than 25 eV

between PBE and BHLYP - whereas the GW self-energy eliminates this functional dependence and brings the G_0W_0 values close to experiment. Further self-consistency does not improve the agreement, suggesting G_0W_0 as the best compromise.
The optical spectra sharpen the same picture, distinguishing what the calculation controls and what is instead intrinsic to this approach. The comparison between the first excitation of H_2O at 10.98 eV within RPA@DFT and at 6.89 eV within BSE@G_nW_0 shows that the downward shift cannot be attributed to the quasiparticle starting point, which opens the gap, but is instead dominated by the attractive electron-hole interaction $-W$ included in the full BSE. Once the sum over virtual states is saturated, the residual basis-set dependence splits the spectrum in two regimes: the bound excitations genuinely converge, agreeing to 0.1 eV across the augmented bases, while the region above the ionization energy never settles. This is a structural limit, since continuum final states cannot be represented by a finite set of localized Gaussians.
Furthermore, the Tamm-Dancoff approximation closely reproduces the BSE results, apart from a slight difference in the peak intensities, because the coupling it sets to 0 is actually negligible in these finite systems. The scissor approximation, instead, replaces the quasiparticle correction with a rigid shift, and shows good agreement with the BSE spectra near the onset but diverges at higher energies, since the actual correction is state-dependent.
The core spectra follow the same physics, but converge more easily. Both the initial $1s$ orbital and the near-edge final states are spatially compact, requiring only a few virtual states, so that the convergence in n_{vw} is fast, the K-edge position is stable, and, as for the valence spectra, the bound resonances converge with the basis while the continuum ones do not.
The approximations behave as in the valence region: the TDA results match the BSE closely, placing the peaks to within 0.01 eV, while the scissor approximation systematically underestimates the transition energies by 0.6 to 1 eV. Compared to experimental values, the BSE@G_nW_0 K-edges fall within 0.4 eV of them. Moreover, adding a relativistic correction to the $1s$ level brings H_2O into almost exact agreement but worsens it for the two carbon edges of CH_4 and C_2H_4, showing that the residual deviations do not arise from relativistic corrections. The finest test is CH_4, as the calculation places the dipole-forbidden transition at 287.07 eV while the measured value is 287.05 eV, and reproduces the correct ordering and different intensities of the two lowest excitations.
Finally, future studies could address what has been found to limit this work. The continuum of states is inaccessible to a localized Gaussian basis, so that only the bound region of the spectra converges. Appropriately describing the continuum and the transitions into it would require methods designed for unbound states, such as plane-wave approaches. Furthermore, the valence GW gap converges slowly with the number of virtual states, and the vibronic and relativistic contributions to the core transitions, necessary for a more quantitative comparison with experiments, lie outside the electronic-structure treatment adopted throughout this thesis.

Above all, the natural continuation of this work is to apply the scheme and approximations now validated on these well-known molecules to larger and more complex systems, for which the setup discussed here offers a reliable starting point.

Acknowledgements

First and foremost, I would like to express my sincere gratitude to my advisor, Prof. Margherita Marsili, for her invaluable patience and constant support throughout the development of this work.
I could not be more grateful to my family for their unwavering love, support, and belief in me, especially over the past two years.
I am deeply grateful to my friends Alice, Matteo, and Elisa for always being there for me. I would also like to thank Davide, Leonardo, Enrico, and Francesco for our friendship and mutual support over the past two years. Finally, I would like to thank Ilaria for her support throughout these years.

Bibliography

[1] Simone Pistillo, Giulia Dall'Osto, Leonardo Biancorosso, Daniele Toffoli, Giovanna Fronzoni, and Emanuele Coccia. Simulating closed- and open-quantum photoinduced electron dynamics for time-resolved NEXAFS. *The Journal of Chemical Physics*, 2026.

[2] Yoshifumi Noguchi, Miyabi Hiyama, Hidefumi Akiyama, Yoshihisa Harada, and Nobuaki Koga. First-Principles Investigation of Strong Excitonic Effects in Oxygen 1s X-ray Absorption Spectra. *Journal of Chemical Theory and Computation*, 2015.

[3] Margherita Marsili and Stefano Corni. Electronic Dynamics of a Molecular System Coupled to a Plasmonic Nanoparticle Combining the Polarizable Continuum Model and Many-Body Perturbation Theory. *The Journal of Physical Chemistry C*, 2022.

[4] F. Sottile. *Response functions of semiconductors and insulators: from the Bethe-Salpeter equation to time-dependent density functional theory.* PhD thesis, École Polytechnique, 2003.

[5] J. Toulouse. Introduction to density-functional theory, 2024. Lecture notes, Sorbonne Université.

[6] P. Hohenberg and W. Kohn. Inhomogeneous Electron Gas. *Physical Review*, 136:B864, November 1964.

[7] K. Capelle, C. A. Ullrich, and G. Vignale. Degenerate ground states and nonunique potentials: Breakdown and restoration of density functionals. *Physical Review A*, 76:012508, 2007.

[8] Mel Levy. Universal variational functionals of electron densities, first-order density matrices, and natural spin-orbitals and solution of the v-representability problem. *Proceedings of the National Academy of Sciences*, 76:6062–6065, 1979.

[9] Mel Levy. Electron densities in search of Hamiltonians. *Physical Review A*, 26:1200–1208, 1982.

[10] Elliott H. Lieb. Density functionals for Coulomb systems. *International Journal of Quantum Chemistry*, 24:243–277, 1983.

[11] W. Kohn and L. J. Sham. Self-Consistent Equations Including Exchange and Correlation Effects. *Physical Review*, 140:A1133, 1965.

[12] D. M. Ceperley and B. J. Alder. Ground State of the Electron Gas by a Stochastic Method. *Physical Review Letters*, 45:566, 1980.

[13] J. P. Perdew and A. Zunger. Self-interaction correction to density-functional approximations for many-electron systems. *Physical Review B*, 23:5048, 1981.

[14] John P. Perdew, Kieron Burke, and Matthias Ernzerhof. Generalized Gradient Approximation Made Simple. *Physical Review Letters*, 77:3865, 1996.

[15] K. Konishi and G. Paffuti. *Quantum Mechanics: A New Introduction*. Cambridge University Press, 2009.

[16] M. Marsili. *Electronic and optical properties of the (111)2×1 diamond surface: an ab-initio study*. PhD thesis, Università degli Studi di Roma "Tor Vergata", 2005.

[17] F. Bruneval and M. Gatti. Quasiparticle Self-Consistent GW Method for the Spectral Properties of Complex Materials. *Topics in Current Chemistry*, 2014.

[18] Fabien Bruneval. *Exchange and Correlation in the Electronic Structure of Solids, from Silicon to Cuprous Oxide: GW Approximation and beyond*. PhD thesis, École Polytechnique, 2005.

[19] Julien Toulouse. Introduction to many-body Green-function theory, 2019. Lecture notes, Sorbonne Université.

[20] Friedhelm Bechstedt. *Many-Body Approach to Electronic Excitations: Concepts and Applications*. Springer, 2015.

[21] Lorenzo Sponza. *Damping, satellites and multiple excitations in oxides and nanostructures: efficient theoretical and numerical approaches towards a dynamical many-body theory*. PhD thesis, École Polytechnique, 2013.

[22] F. Bruneval, Tonatiuh Rangel, Samia M. Hamed, Meiyue Shao, Chao Yang, and Jeffrey B. Neaton. MOLGW 1: Many-body perturbation theory software for atoms, molecules, and clusters. *Computer Physics Communications*, 2016.

[23] E. Aprà, E. J. Bylaska, W. A. de Jong, N. Govind, K. Kowalski, T. P. Straatsma, M. Valiev, H. J. J. van Dam, Y. Alexeev, J. Anchell, V. Anisimov, F. W. Aquino, R. Atta-Fynn, J. Autschbach, N. P. Bauman, J. C. Becca, D. E. Bernholdt,

K. Bhaskaran-Nair, S. Bogatko, P. Borowski, J. Boschen, J. Brabec, A. Bruner, E. Cauët, Y. Chen, G. N. Chuev, C. J. Cramer, J. Daily, M. J. O. Deegan, T. H. Dunning, M. Dupuis, K. G. Dyall, G. I. Fann, S. A. Fischer, A. Fonari, H. Früchtl, L. Gagliardi, J. Garza, N. Gawande, S. Ghosh, K. Glaesemann, A. W. Götz, J. Hammond, V. Helms, E. D. Hermes, K. Hirao, S. Hirata, M. Jacquelin, L. Jensen, B. G. Johnson, H. Jónsson, R. A. Kendall, M. Klemm, R. Kobayashi, V. Konkov, S. Krishnamoorthy, M. Krishnan, Z. Lin, R. D. Lins, R. J. Littlefield, A. J. Logsdail, K. Lopata, W. Ma, A. V. Marenich, J. Martin del Campo, D. Mejia-Rodriguez, J. E. Moore, J. M. Mullin, T. Nakajima, D. R. Nascimento, J. A. Nichols, P. J. Nichols, J. Nieplocha, A. Otero-de-la Roza, B. Palmer, A. Panyala, T. Pirojsirikul, B. Peng, R. Peverati, J. Pittner, L. Pollack, R. M. Richard, P. Sadayappan, G. C. Schatz, W. A. Shelton, D. W. Silverstein, D. M. A. Smith, T. A. Soares, D. Song, M. Swart, H. L. Taylor, G. S. Thomas, V. Tipparaju, D. G. Truhlar, K. Tsemekhman, T. Van Voorhis, Á. Vázquez-Mayagoitia, P. Verma, O. Villa, A. Vishnu, K. D. Vogiatzis, D. Wang, J. H. Weare, M. J. Williamson, T. L. Windus, K. Woliński, A. T. Wong, Q. Wu, C. Yang, Q. Yu, M. Zacharias, Z. Zhang, Y. Zhao, and R. J. Harrison. NWChem: Past, present, and future. *The Journal of Chemical Physics*, May 2020.

[24] Peter J. Linstrom and William G. Mallard. NIST Chemistry WebBook, NIST Standard Reference Database Number 69. National Institute of Standards and Technology, Gaithersburg, MD, 2023. Consultato nel 2026.

[25] National Institute of Standards and Technology. Computational Chemistry Comparison and Benchmark Database, NIST Standard Reference Database Number 101. Release 22, maggio 2022, 2022. Consultato nel 2026.

[26] Frank Jensen. *Introduction to Computational Chemistry*. Wiley, 3rd edition, 2017.

[27] Weiwei Gao and James R. Chelikowsky. Real-Space Based Benchmark of G_0W_0 Calculations on GW100: Effects of Semicore Orbitals and Orbital Reordering. *Journal of Chemical Theory and Computation*, 2019.

[28] Dorothea Golze, Levi Keller, and Patrick Rinke. Accurate Absolute and Relative Core-Level Binding Energies from GW. *The Journal of Physical Chemistry Letters*, 2020.

[29] V. Myrseth, J. D. Bozek, E. Kukk, L. J. Sæthre, and T. D. Thomas. Adiabatic and vertical carbon 1s ionization energies in representative small molecules. *Journal of Electron Spectroscopy and Related Phenomena*, 2002.

[30] Jiachen Li, Ye Jin, Patrick Rinke, Weitao Yang, and Dorothea Golze. Benchmark of GW Methods for Core-Level Binding Energies. *Journal of Chemical Theory and Computation*, 2022.

[31] Emanuele Maggio, Peitao Liu, Michiel J. van Setten, and Georg Kresse. GW100: A Plane Wave Perspective for Small Molecules. *Journal of Chemical Theory and Computation*, 2017.

[32] Yi Yao, Dorothea Golze, Patrick Rinke, Volker Blum, and Yosuke Kanai. All-Electron BSE@GW Method for K-Edge Core Electron Excitation Energies. *Journal of Chemical Theory and Computation*, 2022.

[33] M. Tronc, G. C. King, and F. H. Read. Carbon K-shell excitation in small molecules by high-resolution electron impact. *Journal of Physics B: Atomic and Molecular Physics*, 1979.

[34] Levi Keller, Volker Blum, Patrick Rinke, and Dorothea Golze. Relativistic correction scheme for core-level binding energies from GW. *The Journal of Chemical Physics*, 2020.

[35] Francesco Sottile. *Correlazione elettronica in sistemi a pochi elettroni: studio computazionale con teoria del funzionale della densità e Quantum Monte-Carlo*. PhD thesis, Università degli Studi di Messina, 1999.

[36] G. Giuliani and G. Vignale. *Quantum Theory of the Electron Liquid*. Cambridge University Press, 2008.

[37] David Tong. Kinetic Theory, 2012. University of Cambridge Graduate Course, Department of Applied Mathematics and Theoretical Physics.

[38] Fabio Ortolani. Appunti di Metodi Matematici, 2013. Dispense del corso, 19 febbraio 2013.

[39] R. van Leeuwen and G. Stefanucci. *Nonequilibrium Many-Body Theory of Quantum Systems*. Cambridge University Press, 2013.

[40] J. J. Sakurai and J. Napolitano. *Modern Quantum Mechanics*. Cambridge University Press, 2021.

[41] J. Tempere and G. Kresse. Course notes for Solid State Physics 2, 2020. University of Vienna, Faculty of Physics and Computational Materials Physics.

[42] Margherita Marsili. Theoretical Description of Photoinduced Phenomena: From the Basic Theory to Real-Time Electronic Dynamics in Complex Systems. Presentazione orale, Ladies' Day 2024 - FOR 2824, 2024. Università di Bologna.

[43] Davide Sangalli. Metodi innovativi per il calcolo della risposta lineare nell'ambito della teoria del funzionale della densità in sistemi spin polarizzati, 2012. arXiv:1208.3152.

[44] Petter Minnhagen. Vertex correction calculations for an electron gas. *Journal of Physics C: Solid State Physics*, 1974.

[45] Arno Schindlmayr, Thomas J. Pollehn, and R. W. Godby. Spectra and total energies from self-consistent many-body perturbation theory. *Physical Review B*, 58:12684, 1998.

[46] L. Varrassi. Optical properties of transition metal oxide perovskites by the Bethe-Salpeter equation. Master's thesis, Università di Bologna, 2019.

[47] R. M. Martin, L. Reining, and D. M. Ceperley. *Interacting Electrons: Theory and Computational Approaches*. Cambridge University Press, 2016.

[48] Gianluca Strinati. Application of the Green's Functions Method to the Study of the Optical Properties of Semiconductors. *Rivista del Nuovo Cimento*, 1988.

[49] Xavier Blase, Ivan Duchemin, Denis Jacquemin, and Pierre-François Loos. The Bethe–Salpeter Equation Formalism: From Physics to Chemistry. *The Journal of Physical Chemistry Letters*, 2020.

[50] Marcus Annegarn, Juhan Matthias Kahk, and Johannes Lischner. Combining Time-Dependent Density Functional Theory and the ΔSCF Approach for Accurate Core-Electron Spectra. *Journal of Chemical Theory and Computation*, 2022.

[51] Dorothea Golze, Jan Wilhelm, Michiel J. van Setten, and Patrick Rinke. Core-Level Binding Energies from GW: An Efficient Full-Frequency Approach within a Localized Basis. *Journal of Chemical Theory and Computation*, 2018.

[52] Enrico Ridente, Diptarka Hait, Eric A. Haugen, Andrew D. Ross, Daniel M. Neumark, Martin Head-Gordon, and Stephen R. Leone. Femtosecond symmetry breaking and coherent relaxation of methane cations via X-ray spectroscopy. *Science*, 2023.

[53] Iffat H. Nayyar, Artem E. Masunov, and Sergei Tretiak. Comparison of TD-DFT Methods for the Calculation of Two-Photon Absorption Spectra of Oligophenylvinylenes. *The Journal of Physical Chemistry C*, 2013.